TÉCNICO LISBOA

Cell irradiation dosimetry at the Portuguese Research Reactor in the frame of Boron Neutron Capture Therapy

Maxime Lamotte

Thesis to obtain the Master of Science Degree in

Energy Engineering and Management

Supervisors: Dr. Ana Cristina Fidalgo Palma Fernandes
Prof. Patrícia Carla Serrano Gonçalves

Examination Committee

Chairperson : Prof. Luís Filipe Moreira Mendes
Supervisor: Dr. Ana Cristina Fidalgo Palma Fernandes
Member of the Committee: Prof. Alessandro Esposito

December 2016

Acknowledgment

This work is the fruit resulting of the collaboration and expertise of the numerous people I hereby render thanks. Among the myriad of individuals necessary for the conduction of such remarkable experiments, singular attention is dedicated to the following;

To José Marques for providing me several years of nuclear knowledge across his courses, facilitating and accepting my work at the IST-CTN.

To Nuno Barradas for its help along the numerous experiments held on the reactor.

To Andreas Kling for his knowledge in physics, and its readiness to clarify my doubts.

To Joana Santos for her appreciated technical skills, prompt answers, sympathy and devotion.

To Ana Belchior for her patient explanations of the biological aspects of this work, and her mastering to conduct experiments.

To Patricia Gonçalves for her precious and countless help and in the field of the GEANT4 code, particle physics, metrology and her pedagogy.

To Fernanda Marques and her devotion to BNC studies, her implication in the biological and chemical aspects of this work. Fernanda was the keystone linking our respective fields of expertise.

To Ana Fernandes I dedicate my gratitude, thankfulness and recognition, for the time spent on this work, her dedication on the reactor activities, her confidence and generosity. Over the 8 months necessary for the completion of this valuable work, each day was a pleasure and an enrichment shared with Ana.

Abstract

The present work aims to perform the dosimetry and microdosimetry of cell irradiations at the Portuguese Research Reactor (RPI), in the scope of ongoing research at IST-CTN for the development and *in-vitro* evaluation of novel Boron-loaded compounds for Boron Neutron Capture Therapy (BNCT). We report the dosimetric characterization of irradiation facility at the vertical access of the RPI thermal column. Experimental methods for dose measurement and monitoring of cell irradiations were based on neutron foil activation and thermoluminescent photon dosimetry. The Monte-Carlo particle transport simulation code MCNPX was used for a fine characterization of the mixed radiation field based on a detailed model of the irradiation facility coupled to an existing reactor core model. Simulations were extended to the evaluation of doses in cell structures using the Monte-Carlo GEANT4 code, aiming at a correlation with the observed cell damage.

At maximum reactor power, neutron fluence rates (averaged over the irradiation cavity) are $\phi_0=6.6\text{x}10^7$ cm^{-2} s^{-1} (thermal) and $\theta=2.4\text{x}10^4$ cm^{-2} s^{-1} with a photon dose rate of 150 $mGyh^{-1}$. These values agree with simulations within 85% (thermal neutrons) 78 % (epithermal neutrons) and 95% (photons) thereby validating the MCNPX model.

The GEANT4 simulations, based on a realistic cell model and measured boron concentrations, show that >95% of the dose in cells is due to the BNC reaction. A correlation with the radiobiology studies demonstrates that damage is mostly induced by the incorporated boron, with negligible contribution from the culture medium and adjacent cells, and evidence an extranuclear cell radiosensitivity.

Keywords: BNCT, nuclear reactor, activation foils, thermoluminescent dosimetry, MCNPX, GEANT4

Resumo

Este trabalho visa a dosimetria e microdosimetria de irradiações de culturas celulares no Reactor Português de Investigação (RPI), no contexto do desenvolvimento e avaliação *in-vitro* de novos compostos borados com potencial aplicação em Terapia por Captura de Neutrões em Boro (BNCT). O feixe de neutrões, localizado no acesso vertical da coluna térmica do RPI, foi caracterizado experimentalmente pelos métodos de activação com neutrões e dosimetria por termoluminescência. Foram desenvolvidos modelos para a caracterização mais detalhada do campo de radiações do feixe (utilizando o código MCNPX) e para a determinação da dose de radiação mas estruturas celulares (com o código GEANT4).

Os débitos de fluência de neutrões médios no local de irradiação das células (à potência máxima do reactor) são ϕ_0=6.6x10^7 cm^{-2}s^{-1} (térmicos), θ=2.4x10^4 cm^{-2}s^{-1} (epitérmicos); o débito de dose de fotões é 150 mGyh^{-1}. O acordo com os valores calculados é de 85% (térmicos), 78% (epitérmicos) e 95% (fotões), validando assim o modelo MCNPX.

A simulação das células considera um modelo geométrico realista com uma distribuição de Boro nas estruturas celulares determinada experimentalmente. A correlação com estudos de radiobiologia mostra que o dano é principalmente produzido pelo Boro incorporado na própria célula, e que a assimilação dentro do núcleo não é essencial para a indução de efeitos genéticos.

Palavras-chave: BNCT, reactor nuclear, detectores de activação, dosimetria por termoluminescência, MCNPX, GEANT4

Contents

Figures and tables

Abbreviations

BBB: Blood-brain barrier

BNCT: Boron Neutron Capture Therapy

BPA: boronophenylalanine

BSH: sodium borocaptate

CAD: Computer Aided Design

CERN : Centre Européen de la Recherche Nucléaire

CMA: Carboranylmethylbenzoacridone

DNA: Deoxyribonucleic acid

DSB: Double Strand Break

GBM: Glioblastoma Multiforme

GEANT4: Geometry ANd Tracking 4

HPGe: High Purity Germanium Detector

ICP-MS: Inductively Coupled Plasma Mass Spectrometry

IST-CTN: Instituto Superior Técnico – Campus Tecnológico e Nuclear

Kerma: Kinetic Energy Released in Matter

LET: Linear Energy Transfer

MCA: Multiple Channel Analyser

MCNP : Monte Carlo N-Particle eXtended

MN: Micronucleus

MTT: (3-(4,5-dimethylthiazol-2-yl)-5-(3-carboxymethoxyphenyl)-2-(4-sulfophenyl)-2H-tetrazolium)

PBS: Phosphate-buffered saline

PMT: PhotoMultiplier Tube

RBE: Relative Biological Effectiveness

RPI: Reactor Português de Investigação

TLD: Thermoluminescent Dosimetry

WW: Weight Window

1 Introduction

1.1 Motivations and objectives

Glioblastoma multiforme (GBM) represents 15-20% of primary intracranial brain tumours diagnosed on about 10 000 patients every year. In addition to a main massive part GBM contains tentacle-shaped structures that are difficult to remove completely by surgery (ABTA, 2012). Radiotherapy and chemotherapy are applied allowing to reduce tumour growth. However, recurrence at the original tumour location is very frequent, displaying a lack of effectiveness for these treatments. GBM remains as a disease of poor prognostic, with a median survival rate of 10-12 months after treatment.

Boron Neutron Capture Therapy (BNCT) emerged as an alternative treatment modality with a primary focus on GBM. BNCT is a binary therapy relying on the association of two non-cytotoxic components, boron compounds and thermal neutrons. As current nuclear reactor facilities involved in clinical trials fulfil the dosimetric requirements, developments in BNCT are focussed on the drug delivery component. Tumour-targeting properties are crucial parameters for the sparing of safe tissues, and the positive outcome of the therapy.

In this context, research groups in IST-CTN currently develop new boron compounds based on DNA-intercalator and boron clusters for potential application in BNCT and performs their *in-vitro* evaluation. The present works aims at characterizing the irradiation facility of the Portuguese Research Reactor employed in cell irradiations using carboranylmethylbenzoacridones derivatives as novel agents. The characterisation is enhanced with microdosimetric simulations allowing to derive the dose components in the various cell structures towards a correlation with the observed cell damage.

1.2 Boron Neutron Capture Therapy

BNCT is a binary therapeutic modality as the patient is irradiated with low-energy neutrons (thermal neutrons, n_{th}, with energy <0.5eV) after administration of a tumour-seeking compound containing ^{10}B (Barth et al, 2009). Each component is essentially non-cytotoxic (thermal neutrons have insufficient velocity to cause appreciable damage in tissue (Coderre, 1999)) but their combination sensitises the compound leading to cell destruction (Figure 1-1).

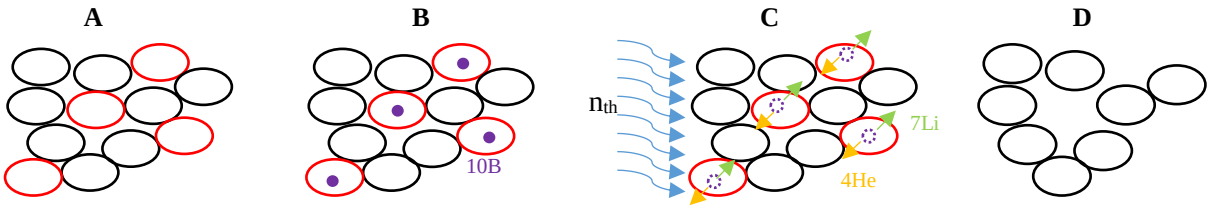

Figure 1-1 Principle of BNCT. (A) Tumour (red) and normal (black) cells. (B) Cells containing a boronated compound. (C) Under thermal neutron fluence rate, ^{10}B produces ^{7}Li and ^{2}He fragments of high velocity. (D) Normal cells surrounding the tumour are spared while tumoural cells cannot repair their damages.

The ^{10}B isotope, occurring naturally at 19.8% in Boron, has a large capture cross-section to low-energy neutrons. The absorption cross section at 25 meV is 3870barn *vis-à-vis* 0.333barn for H that has the highest atomic density in tissue. Neutron capture by ^{10}B occurs through an (n,α) reaction leading to an unstable ^{11}B that decays

releasing 2.79MeV. This energy is shared between ^{4}He (alpha particle, α) and ^{7}Li nuclei, and in 93.7% of the cases, also with a 478keV photon.

$$^{10}B + n_{th} \rightarrow {}^4He\ (1.47MeV) + {}^7Li\ (0.84MeV) + \gamma(0.48MeV)\ \ (93.7\%) \qquad \text{(eq.1)}$$

$$^{10}B + n_{th} \rightarrow {}^4He\ (1.78MeV) + {}^7Li(1.47MeV)\ \ (6.3\%) \qquad \text{(eq.2)}$$

The α and Li fragments have a range in water of 5-10μm, which is the typical dimension of cells. The rationale for BNCT is based on the concept that, once ^{10}B is incorporated exclusively in the tumour cells, these will be killed by the high energy deposited by the BNC products whilst sparing the surrounding healthy tissues (Barth et al, 2009).

The first clinical trials of BNCT were carried out in USA in the early 1950's, using a thermal neutron beam and borax or $Na_2B_{10}H_{10}$ (less toxic than borax) as Boron compound. These trials were unsuccessful, as the compounds were not selective for tumour tissue, and trials were halt after 10 years. In the late 1960's, trials started in Japan using $Na_2B_{12}H_{11}SH$ (sodium borocaptate, BSH) as an improved compound shown to accumulate selectively in mouse glioma cells. The treatment was performed after tumour excision as an intra-operative radiotherapy, where the tumour bed was exposed directly to the thermal neutron beam. The encouraging results led to the treatment of superficial melanoma with a different compound (boronophenylalanine, BPA) and to the reconsideration of clinical application with BNCT in the USA, as well as in Europe. In the 1990-2000's, clinical trials in other countries (USA, UK, Netherlands, Finland, Sweden, Czech Republic, Argentina, Italy, Taiwan) were performed at research reactor facilities using post-operative irradiations with epithermal neutron beams (0.5eV-10keV) that give much better neutron penetration in tissue and thermalize at 2-3 cm depth. The application extended from recurrent to newly diagnosed GBM, inoperable and recurrent head and neck cancer, extensive radio- and/or chemo-resistant malignancies in head and neck, malignant meningioma, recurrent glioma, hepatic, gastrointestinal and lung cancer. The most consistent trials in Europe were stopped: in the Netherlands, BSH did not demonstrate sufficient uptake and selectiveness; the outcome of trials in Finland and Sweden employing BPA was generally positive and apparently, the decision to interrupt the activity in the late 2000's was based on financial criteria. The main activity continues to be carried out in Japan.

1.3 Neutron compounds, neutron sources and dosimetry

In-vitro evaluations show that effective killing requires that the cell contains at least 10^9 ^{10}B atoms and is irradiated with a thermal neutron fluence of ~$5x10^{12}$ $n_{th}cm^{-2}$; this corresponds to a mass concentration of ~20ppm ^{10}B and leads to ~10 BNC reactions in a cell of 0.5ng mass (Barth et al, 2005). For a tolerable treatment toxicity, a targeting tumour-to-normal-tissues with a ratio as high as 3 is required for the Boron delivery agent. BPA and BSH (2nd generation compounds, after the 1st generation of non-selective carriers) remain as the only two compounds approved for clinical use, each one with advantages and disadvantages. BSH is a small molecule able to cross the blood-brain barrier (BBB, a membrane-like structure that protects the brain from toxic substances present in the blood) often disrupted by the tumour. BSH is retained longer in the brain than in blood; however, *in-vivo* measurements of tumour-to-normal concentration ratios yield extremely variable results (2 to 10) and evidence a very high concentration in neighbouring organs that do not have a BBB (eyes and superficial tissue). BPA crosses the BBB and accumulates in GBM at with a selectivity of ~3.5, but exhibits a very heterogeneous distribution; still it is currently the most used compound. These molecules display a low penetration in the nuclei

of cells as well as low ability to cross the blood-to-brain cancer and a reduced solubility in water, thus, making them relatively inefficient (Lu et al., 1997).

Over the last decade, boron carrier development has taken two directions: small boron molecules and boron-conjugated biological complexes. A promising route is the incorporation of boron delivery agents into tumour-targeting molecules such as peptides, proteins, anti-bodies, nucleosides, sugars, porphyrins and liposomes, whilst another is optimisation of the administration method. One of the more promising routes would appear to be nanoscale drug delivery systems using liposomes and nanoparticles.

The new compounds studied in this paper rely on boron atomic clusters to carry more atoms (up to 10) in a non-cytotoxic molecule. Dodecarborane appears as a good cluster as it remains stable in biological environment. DNA-binding agents (3rd generation boron compounds), associated with tumour-targeting molecules and boron clusters can strongly improve the efficiency of BNCT over classical delivery agents (Crossley, 2007). The compounds used in this work employ (-acridone derivatives) as DNA intercalator and, in addition, are of interest for PhotoDynamic Therapy (Serra et al., 2010).

Neutrons are the other important agent in BNCT. Most neutron sources have relied on thermal or epithermal beams at research reactors. These beams are produced by filtering the neutrons from the reactor core; for low power reactors, a ^{235}U fission converter can be used to increase the beam output away from the core (Riley et al, 2003). Research reactors are expensive facilities that raise various safety concerns to the public, and are usually located away from medical centres. A new type of reactor, compact, passive and intrinsically safe relies on core neutrons for in-hospital use (Li et al, 2010) allowing a convenient patient irradiation with minimal logistic. Accelerator-based neutron sources present a viable alternative. The simplest solution relies on the incidence of a 2.5MeV proton beams on a ^{7}Li enriched target to produce neutrons with the average energy of 400keV (Blue et al, 2003). Relative to reactors, less moderation is required to achieve the intended neutron energy range, leading to higher fluence rate and compacticity. Japan currently develops accelerator based neutron sources for clinical use (Yohioka et al., 2014).

It is generally considered that the current technology is able to produce neutron beams with the adequate properties for BNCT in terms of fluence rate, neutron energy and contamination by other radiation types. A joint European effort was made to recommend the methods and attainable uncertainties for the dosimetry in BNCT. It has been recognised that due to the complexity of the radiation field, the accuracy of the dose delivery to a patient required in radiotherapy is difficult to achieve in BNCT applications (Stecher-Rasmussen et al., 1997). For that reason, the need to compare the results of dosimetric measurements with supporting calculations was greatly emphasised. As a corollary, improved accuracy on the assessment of *in-vivo* boron concentration distribution in tissue and treatment planning systems is mandatory.

1.4 Relation to previous work

The Reactor Português de Investigação (RPI) has been involved in several activities in the context of BNCT since the 1990's with several collaborations with national and European institutions (Alcober et al, 1997). The configuration of the irradiation facility at the vertical access of the thermal column was optimized with a Lead shield in order to reduce the gamma dose, and this facility has been used for thermal neutron irradiation of cell cultures (mainly melanoma A2058 cells loaded with BPA) and small animals (Oliveira et al., 2001) (Irles et al.,

2001). An epithermal beam facility was designed for further BNCT experiments (Gonçalves, 1997) (Gonçalves et al, 1998) (Albornoz et al., 2005).

Thermal and epithermal neutron fluences in air were measured with activation foils, and results were extrapolated to the sample irradiations. Early attempts to simulate the whole neutron and photon spectrum were made based on the first Monte Carlo model of the reactor core (using the MCNP code) that included fuel at a high burnup. The model failed to estimate the absolute fluence rate values and predicted a thermal-to-epithermal ratio two times higher than measured. The simulations also suffered from poor statistical uncertainty due to the reduced computational capability at the time. Nevertheless, when results were normalized to the measured thermal neutron fluence rate at one point, spatial distributions of neutron fluences and photon doses were successfully retrieved. The thermoluminescent dosimetry method was implemented for dose assessment in the mixed (neutron+photon) radiation field.

In-vitro studies were resumed after a gap of 10 years. Experiments are now progressing with GBM cells and with the novel dodecarborane compounds. The simulation of the radiation field in the vertical access of the thermal column, partly recovered from the previous work, includes revised material data and is coupled to a reactor core model validated for the determination of absolute neutron fluence rate values (Fernandes et al., 2010). The Monte Carlo GEANT4 code is used for the first time to support the dosimetry of cell irradiations at the RPI. The effect of the irradiated samples over the neutron field is considered, allowing to derive the doses induced by the various nuclear reactions – namely BNC – and by the photon background. The dose in cell structures is calculated with a microdosimetric model, and the results are correlated with the observed biological effects.

1.5 Structure of the present work

The present work is divided in 5 chapters: an introduction presenting challenges and opportunities of the reactor dosimetry and BNCT drug delivery agents faced by the research team of the CTN. Theoretical considerations are presented in chapter 2, to interpret obtained results. Chapter 3 describes materials, codes and equipment used, their respective procedures and methodologies. Chapter 4 presents the results obtained with respect to equipment calibration, dose measurements in the irradiation facility, Monte-Carlo simulations and biological assays. Finally, chapter 5 offers a general conclusion and discussion of the results focusing on the irradiation facility characterization, and the radiobiological outcomes of the irradiated glioblastoma cells.

2 Theoretical background

2.1 Radiation field in a moderated fission reactor

Various types of radiation are present in a nuclear reactor (Treille, 1963): heavy ions and neutrons as fission products, alpha particles from the decay chains of $^{235/238}$U and minor actinides; beta particles from the decay of fission products and materials activated by neutrons; gamma rays accompanying fission and neutron capture reactions (prompt emission) and emitted during the decay of the radioactive materials (Lemaignan, 2004).

The charged particles (ions, alphas, betas) generated in the fuel are retained within or very close to the fuel elements. In contrast, the neutrons and photons may travel significantly higher distances in other medium. The radiation field at a reactor is generally mixed, with a photon component inseparable from that of neutrons.

The interactions and effects induced by neutrons in a material have a strong dependence on its composition, and also with the neutron energy (E). In a moderated reactor like the RPI neutrons in the energy range of 10^{-9}-10 MeV are present. This large interval is generally divided in three energy regions (of somewhat arbitrary limits) according to the dominant interaction processes:

- Fast neutrons (E>0.1MeV) are generated by the fuel fission. The Watt-Cranberg formula is an empirical distribution that represents the neutron energy spectrum in the 0.5-15MeV energy range, the upper limit corresponding to the maximum energy of ^{235}U fission neutrons (Bussac, 1978).

$$\Phi_{fast}(E) = He^{-1.036E}\sinh\left(\sqrt{2.29E}\right) \quad \text{(eq.3)}$$

  where H is a normalization factor and E is expressed in MeV. Nuclear transmutation and scattering (elastic+inelastic) are the predominant neutron interactions with most materials.

- Epithermal neutrons (0.5eV<E<0.1MeV) result from the slowing-down of fission neutrons. Their theoretical spectrum follows a 1/E function:

$$\Phi_{epi}(E) = \theta/E \quad \text{(eq.4)}$$

  where θ is a normalization factor. Most threshold reactions are no longer possible and elastic scattering (n,n) and resonant radiative neutron capture (n,γ) emerge as the most frequent interaction.

- Thermal neutrons (E<0.5eV) correspond to those in thermal equilibrium with the surrounding moderator material. In the absence of strong absorption, a Maxwell distribution of the spectrum is admitted theoretically

$$\Phi_{th}(E) = \frac{AE}{(kT_n)^2}\, e^{\frac{E}{(kT_n)}} \quad \text{(eq.5)}$$

  where A is a normalization factor, k is the Boltzmann constant and T_n is the neutron temperature, equal to that of the moderator. Elastic scattering and absorption (mainly by (n,γ)) are dominant in this energy range, and even increase at reduced neutron energy. At T_n=293K, the most probable neutron energy and velocity are 25 meV and 2200 ms^{-1}, respectively (Reuss, 2003). When there is a strong absorption (e.g., close to the fuel), a Maxwell distribution is often valid although at a temperature higher than the moderator.

The neutron spectrum is conveniently represented in lethargy units in order to evidence the three energy ranges. Neutron lethargy (u), or logarithmic energy decrement is (Le Sech, 2014)

$$u = \ln(E_0/E) \quad \text{(eq.6)}$$

where E_0 an arbitrary initial energy, and E the current energy after n collisions. The generic shape of the neutron spectrum in a moderated reactor is presented in Figure 2-1.The relative height between the "bumps" at the low and high energy ends indicates the thermal-to-fast fluence ratio, while the horizontal line corresponds to the epithermal fluence rate per unit lethargy, θ.

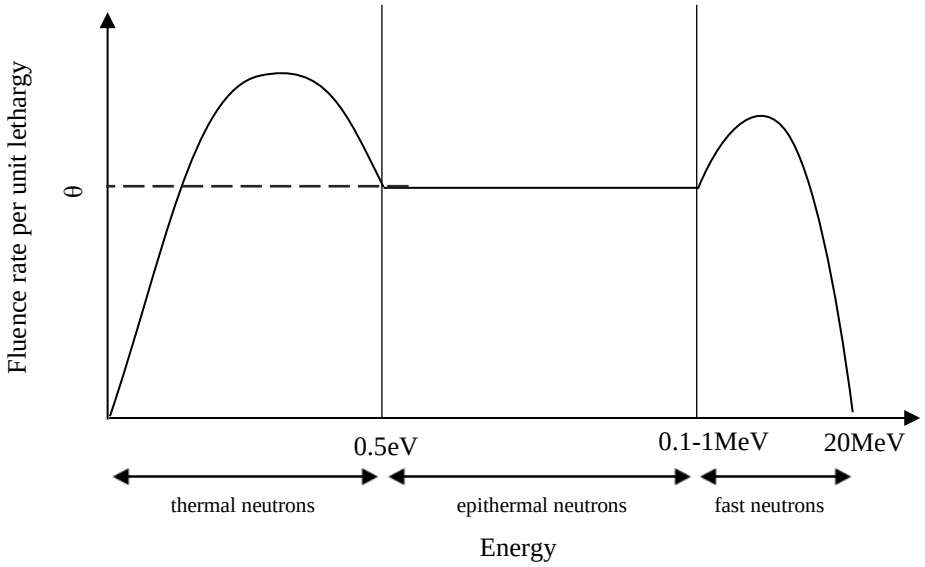

Figure 2-1 Neutron energy distribution (lethargy representation) in a moderated ^{235}U reactor.

The photon spectrum in the core region covers a wide energy range. High energies (5-10 MeV) are generally associated to prompt emission, whereas photons in the order of 1-3 MeV correspond mostly (but not exclusively) to the decay of radioactive products. The intensity of the later has a temporal variation that also depends of the reactor operation history (e.g., power, duration of irradiations, cooling times).

The occurrence of three main photon interactions (photoelectric effect, Compton scattering and pair production above 1.022MeV) is influenced by the medium atomic number and photon energy as shown in Figure 2-2.

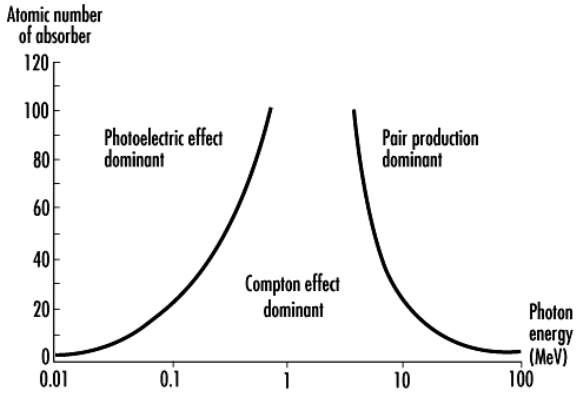

Figure 2-2 Domains of relative importance of photon interaction depending on energy and target material atomic number (adapted from Le Sech, 2014)

2.2 Dosimetric quantities

Ionizing radiation is considered in this work. The absorbed dose at a point in a material is defined as the average energy deposited (ΔE) by mass unit (Δm) following numerous energy deposition processes in an infinitesimal volume around that point.

$$D = \frac{< \Delta E >}{\Delta m} \quad \text{(eq.7)}$$

Neutrons and photons are neutral particles. The energy transfer is a two-step process:

1) The incoming neutral particle generates and transfers its kinetic energy to secondary charged particles in the medium - these can be nuclei or protons in the case of neutrons, or electrons in the case of photons;
2) The secondary charged particles depose their energy after a succession of collisions until rest. There is also a radiative energy loss (*bremsstrahlung* radiation) that is insignificant for particles heavier than the electron.

With respect to step 1), the quantity describing the kinetic energy transferred per unit mass is kerma (kinetic energy transferred in matter). Kerma is expressed in Gray (Gy) but doesn't have the same meaning as absorbed dose, as secondary particles can escape the volume without depositing all their energy in it.

The spatial scale at which the energy is deposited (relative to the track length of the primary particle) is different for neutrons and photons. Nuclei generated by neutrons undergo a reduced number of interactions and deposit their energy locally, whereas the production of electrons may extend "far" from the primary interaction point.

Tabulated flux-to-dose conversion factors can be used to calculate the neutron and photon doses based on the particle and energy fluence, respectively. The photon energy transmitted through a slab of medium is characterised by the linear energy-absorption coefficient μ_{en} (similarly to the attenuation coefficient for the description of particle transmission). The relation between photon dose ($D\gamma$) and photon energy fluence (Ψ_γ) is

$$D_\gamma = \int_0^\infty \Psi_\gamma(E_\gamma) \frac{\mu_{en}}{\rho}(E_\gamma) dE_\gamma \quad \text{(eq.8)}$$

where ρ is the material mass density (in $kg.m^{-3}$).

As neutrons transfer all their kinetic energy locally, neutron dose (D_n) and kerma are coincident, and given by

$$D_n = \int_0^\infty \Phi_n(E_{n)}\, k(E_n) dE_n \quad \text{(eq.9)}$$

where k (kerma factor) is the interaction coefficient that describes the transfer of kinetic energy and Φ_n is the neutron fluence.

The energy deposited in a material can be converted to electric charge, chemical effects, light, atom dislocations, heat, radioactivity, etc. In the case of biological material, the observed ultimate effects of radiation focus on cell death/viability/integrity or, in the case of animals and plants, either the occurrence or the improved resistance against specific diseases.

The different profiles of energy deposition between neutrons and photons explains the different effectiveness and sometimes distinct biological effects of the two radiation types. These must be therefore addressed in the dosimetry of biological material at a reactor.

The Linear Energy Transfer (LET) quantifies the collisional energy loss of a particle in a given material. The LET is the average energy loss per unit length (usually in KeV μm^{-1}). LET is used in the context of radioprotection and radiobiology, when different kinds of radiations are present. Alpha particles have high LET and lead to high radiobiological effects.

The Relative Biological Effectiveness (RBE) is a weighting parameter that compares the effects induced by the same dose of different radiation types or energies, having 250keV x-rays as a reference (RBE=1) (Sinclair et al, 1992). The RBE is often measured *in-vitro*, and is observed to depend on LET for LET>10 $keV\mu m^{-1}$ (IAEA, 1985). Although the RBE depends on the cell type and viability assay, maximum values are generally observed at LET~100 $keV\mu m^{-1}$.

2.3 Monte Carlo simulation of radiation transport

Radiation transport simulation by the Monte Carlo method is based on the simulation of individual particle stories and recording of some aspects of their average behaviour (tallies). The probabilistic interactions involved during the transport of the particle in a medium are simulated sequentially. Random numbers are used to sample the probability distributions governing the occurrence and outcome of the interaction. A normalised random number in the 0-1 range is associated to the cumulative probability distribution (Figure 2-3). In the case of neutrons, random numbers define which reaction takes place - based on the cross sections of all possible reactions (fission, capture…) - the reaction products (defined by branching ratios or emission probabilities), their direction (determined by the angular distribution data) and the track length until the next interaction.

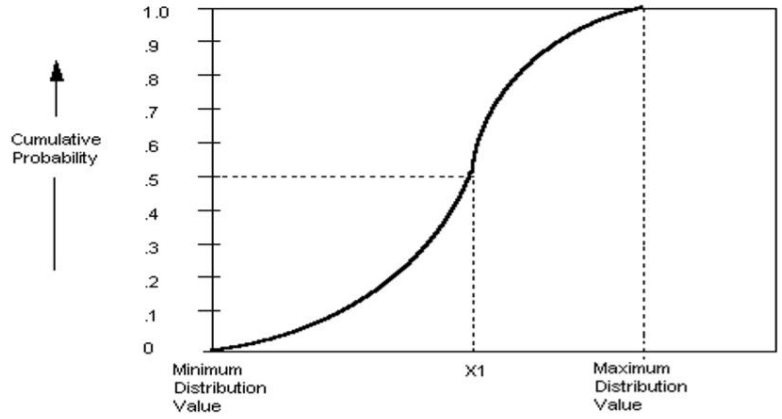

Figure 2-3 Cumulative probability distribution of a quantity. The steeper the curve, the most likely the quantity. Adapted from (Palisade Corporation, 2016)

Monte Carlo methods reproduce the stochastic nature of radiation interactions, and have been extensively developed and employed in the simulation of physical systems in nuclear reactors, medical applications of radiation, design of radiation detectors or post-accident estimates of radioactive contamination. Some of the most popular general-purpose Monte Carlo codes able to deal with neutrons and photons are MCNP, GEANT, FLUKA, TRIPOLI – released with specific random number generator and nuclear data tables.

The number of trials necessary to adequately describe a process is usually quite large. The statistical uncertainty of a result is a function of the number N of contributing events (the relative uncertainty u is $\sim 1/N^{1/2}$), and so on computation time. When the number of particles scored in the volume of interest is very small (e.g., target volumes far away from the source, deep penetration problems, labyrinth-like geometries) variance reduction

techniques are employed. Each code has specific variance reduction techniques implemented, and these will be discussed in Section 3.3.3 for the MCNPX and GEANT4 codes employed in this work.

2.4 Neutron fluence measurement by the activation method

Neutron activation is a standard method for neutron fluence rate measurements in reactors. A small detector (normally circular foils or wires) containing a known mass of the target isotope, is exposed to a neutron field of unknown fluence rate. A series of nuclear reactions may occur, and the reaction rate per target atom R (detector response) is

$$R = \int_0^{+\infty} \sigma(E)\phi(E)dE \qquad \text{(eq.10)}$$

where σ is the reaction cross section and ϕ is the neutron fluence rate.

After irradiation, the radioactivity of the detector induced by the neutrons is measured and the result is used to extract ϕ (Tsoulfanidis N., 1995). The derivation is based on theoretical models for the neutron spectrum and the cross section of the activation reaction, yielding an analytical expression for R.

Radiative capture has big cross sections at low energies being therefore frequently employed to measure neutrons in the thermal and epithermal range whereas threshold reactions (inelastic scattering, (n,p), (n,α)) are considered for fast neutrons.

2.4.1 Radiative capture cross-section

The cross section for the (n,γ) reaction is various isotopes is shown in Figure 2-4. For most isotopes, the cross section consists of a continuous 1/v shape in the thermal region with superimposed resonances in the epithermal range.

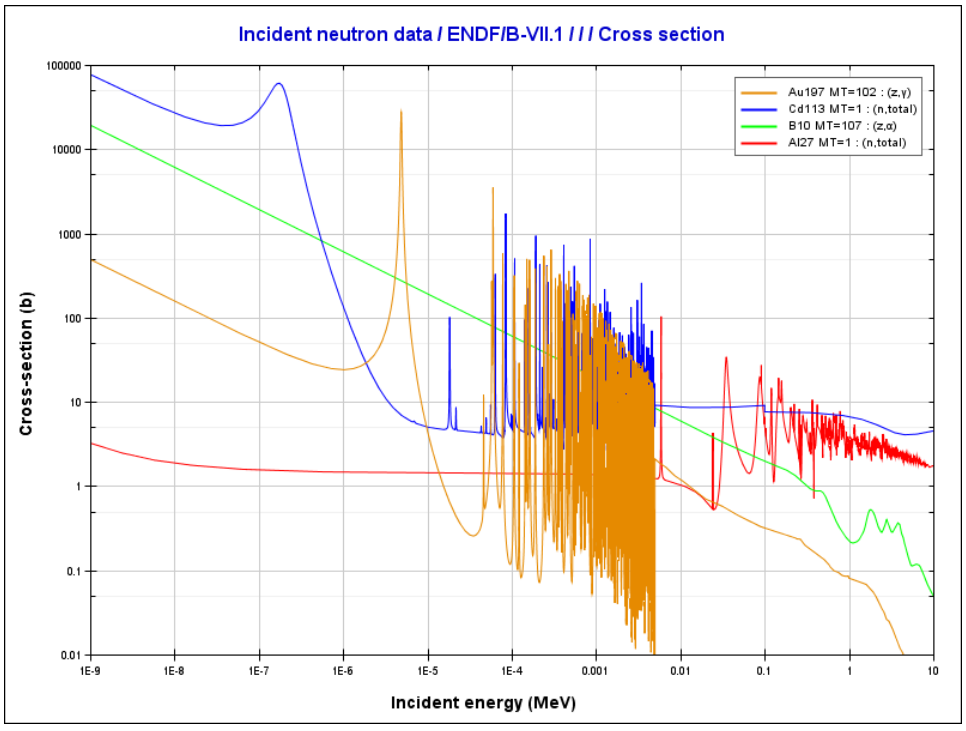

Figure 2-4 Cross sections for: (n,tot) of ^{113}Cd and Al; (n,α) of ^{10}B and (n,γ) of Au; ENDF library via the NEA Janis software (NEA, 2016)

In the 1/v region, $\sigma(E) = \sigma_0\sqrt{E_0/E}$, where σ_0 is the cross section at a reference energy E_0 usually considered as 25 meV. The detector response induced by a thermal neutron field is simply:

$$R_{th} = \sigma_0 \, \phi_0 \quad \text{(eq.11)}$$

where ϕ_0 is the conventional thermal neutron fluence rate corresponding to a monoenergetic neutron beam of v_0=2200ms^{-1} and with the total thermal neutron density (n_{th}), that induces the same response as the actual Maxwell distribution

$$\phi_0 = n_{th} \, v_0 \quad \text{(eq.12)}$$

The relation between the total and conventional thermal neutron fluence rates is (with T_0=293K):

$$\phi_{th} = 2/\sqrt{\pi}\phi_0\sqrt{T_n/T_0} \quad \text{(eq.13)}$$

In practice, there may be a deviation of the cross section from the 1/v distribution. This is taken into account by a multiplicative correction factor to the cross section, the Westcott factor g (Wirtz, 1964) that is tabulated for most reactions employed in reactor dosimetry.

2.4.2 Resonance integral

The resonances in the cross section yield a detector sensitivity to neutrons in the resonance energy region, that can be ultimately extrapolated to the complete 1/E epithermal region. The response induced by epithermal neutrons is

$$R_{epi} = I \, \theta \quad \text{(eq.14)}$$

$$I = \int_{E_{Cd}}^{+\infty} \sigma(E)/_E \, dE \quad \text{(eq.15)}$$

The parameter I is the resonance integral beyond the energy limit that divides the thermal and epithermal regions. This limit is usually selected at the cadmium energy cutoff E_{cd}=0.5eV (IAEA, 1977). Values of I are tabulated for most dosimetric reactions. In the case of ^{197}Au, the resonance is located at 5eV, yielding a sensitivity to neutrons in this energy region.

2.4.3 Neutron self-shielding

The absorption of neutrons by the foil reduces its activation, as the shallow material layer shields the deeper part of the foil against neutrons. This effect is considered by the thermal (G_{th}) and epithermal (G_{epi}) self-shielding factors. These depend on the foil dimensions, is material and concentration. Detectors diluted in aluminium (up to 10%) can be used for negligible self-shielding, but their activation is reduced.

Self-shielding factors have been determined experimentally or by simulation. For thermal neutrons incident on a thin foil of thickness z, the following self-shielding factor expression was used (Martinho et al, 2004):

$$G_{th}(z) = \frac{1}{1 + \left(\frac{z}{1.029}\right)^{1.009}} \quad \text{(eq.16)}$$

$$z = \Sigma_{tot}.y.\sqrt{\frac{\Sigma_{abs}}{\Sigma_{tot}}} \quad \text{(eq.17)}$$

where Σ_{tot} and Σ_{abs} are the total and absorption macroscopic cross sections of the foil material at 25meV. The macroscopic cross section Σ (unit cm^{-1}) is obtained by multiplying the cross section σ by the atomic density (in atoms per cm^3) for each element in the foil.

In the case of epithermal neutrons, the following formula was used to derive G_{epi} within 18% uncertainty (Martinho et al., 2003):

$$G_{epi} = \frac{A_1 - A_2}{1 + \left(\frac{z}{z_0}\right)^p} + A_2 \quad \text{(eq.18)}$$

$$z = \Sigma_{tot}(E_{res}).y.\sqrt{\frac{\Gamma_\gamma}{\Gamma}} \quad \text{(eq.19)}$$

with $A_1 = 1$ $A_2=0.06$ $z_0= 2.7$, p= 0.82 and y= 1.5 thickness.

If various resonances are present, a weighting factor w_i is applied to each:

$$< G_{epi} > = \frac{\sum_{i=1}^{n} w_i \; G_{epi}(z_i)}{\sum_{i=1}^{n} w_i} \quad \text{(eq.20)}$$

$$w_i = \frac{\Gamma_\gamma}{E_{res}^2} \frac{\nabla \Gamma_n}{\Gamma} \quad \text{(eq.21)}$$

$$\nabla = \frac{(2J+1)}{2(2I+1)} \quad \text{(eq.22)}$$

where J is the resonance spin rate, I the spin of the nucleus prior to activation, Γ_n the neutron resonance width - all tabulated. The weighting factor strongly decrease with the energy of the resonance peak, thus, most of the self-shielding is due to the first resonances at low energies.

2.4.4 Cadmium-ratio method

If a detector has a cross-section behaving as 1/v up to 1.5eV, its total response can be stated as:

$$R_{th} + R_{epi} = \frac{g\,\sigma_0\,\phi_0}{G_{th}} + \frac{I\,\theta}{G_{epi}} \quad \text{(eq.23)}$$

The Cadmium-ratio method is based on the application of a filter of Cd in order to discriminate the activation induced by thermal and epithermal neutrons. Cadmium, particularly its 113 isotope, has a very big absorption cross section for thermal neutrons (19969 barns) that drops rapidly at 0.5eV to low values (125 barns at 1eV) (NEA, 2016). This is a good filter of thermal neutrons, as foils irradiated under a Cd cover of 1mm thickness are activated only by epithermal neutrons above the cadmium cut-off E_{Cd}=0.5eV.

In the Cadmium-ratio method, the thermal and epithermal fluence rates are derived from the irradiation of a pair of foils, one covered by Cd and another bare. The response of a Cadmium-covered foil (R_{Cd}) yields θ, and is subtracted to the response of the base foil (R_b) in order to derive ϕ_0.

Because the cadmium absorption cross section is not a step function, a factor F_{cad} is used to correct the effect of the cover for neutrons close to E_{Cd}. This factor is tabulated or measured for each target material, filter thickness and orientation of the neutron field (isotropic *vs.* beam).

The epithermal neutron fluence rate per unit lethargy is:

$$\theta = \frac{R_{Cd} F_{cd}}{I\,G_{epi}} \quad \text{(eq.24)}$$

and the conventional thermal fluence rate is:

$$\phi_0 = \frac{R_b - R_{Cd}F_{cd}}{\sigma_0 g_0 G_{th}} \quad \text{(eq.25)}$$

2.4.5 Activation equation

In the activation method, the foil is irradiated during t_{irr}, and its activity is measured t_{dec} after irradiation. Each disintegration of the reaction product is accompanied by the emission of photons of specific energies (E_γ) and emission probabilities (p_γ). The activity is measured by identifying one of these photons using a gamma spectrometer calibrated for energy and efficiency (η). The measured activity for the photon energy of interest is

$$A_{mes} = {C}/{t_{mes}} \quad \text{(eq.26)}$$

where C is the number of photons and t_{mes} is the live measurement time. The real disintegration rate A_r of the reaction product is

$$A_r = {A_{mes}}/{\eta p_\gamma} \quad \text{(eq.27)}$$

The relation between A_r and the detector response is determined considering the balance between the production of the reaction product during irradiation (given by R) and its decay during and after irradiation (Figure 2-5). During irradiation, the detector activity (per target isotope) approaches a saturation limit given by R that in practice, is never reached. Its relation with the actual activity is

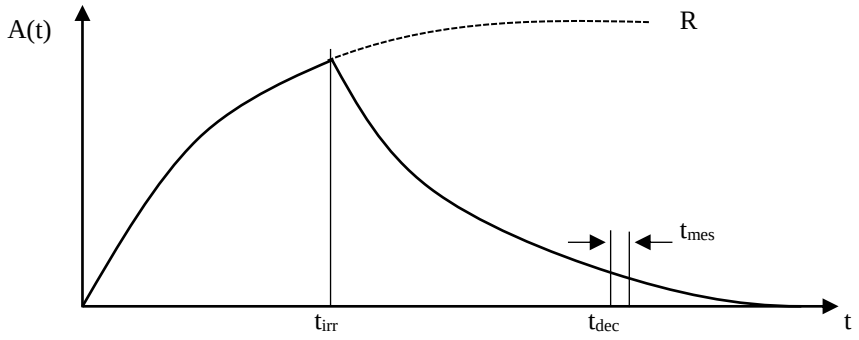

Figure 2-5 Evolution of the sample activity during irradiation, decay and measurement

$$R = \frac{A_r / N_{at}}{F_{irr}\, F_{dec}\, F_{mes}} \quad \text{(eq.28)}$$

$$F_{irr} = 1 - exp^{(-\lambda\, t_{irr})} \quad \text{(eq.29)}$$

$$F_{dec} = exp^{(-\lambda\, t_{dec})} \quad \text{(eq.30)}$$

$$F_{mes} = \frac{1 - exp^{(-\lambda\, t_{mes})}}{-\lambda\, t_{mes}} \quad \text{(eq.31)}$$

In this equation, the irradiation factor F_{irr} corrects for the fact that the irradiation did not last enough time to reach the saturation activity R, the decay factor F_{dec} corrects for the decay between irradiation and activity measurement, F_{mes} considers the decay during the activity measurement. The disintegration constant λ is related to the half-life of the reaction product $T_{1/2}$

$$\lambda = {\ln(2)}/{T_{1/2}} \quad \text{(eq.32)}$$

and the number of target atoms in the foil of mass m is

$$N_{at} = \mathcal{N}_{av} \frac{M}{m} a \qquad \text{(eq.33)}$$

with N_{av} being the Avogadro number, a the atomic abundance of the target isotope in the foil and M its atomic number. For $T_{1/2} >> t_{mes}$, F_{mes} can be approximated to 1.

2.5 Thermoluminescent dosimetry

Thermoluminescence (TL) consists on the release of the energy a material has stored from radiation, in the form of light when heated. When the detected light output is proportional to the dose, the material can be used as a thermoluminescent dosemeter (TLD). Dielectric or semi-conductors may exhibit TL.

In the band model commonly used to describe TL, the zone between the conduction and valence band may include traps, i.e. metastable levels were electrons can rest, if the crystal has imperfections (clusters, dopants, etc). If energy is injected in the crystal (step 1 in Figure 2-6), electrons can jump from conduction to valence band. Later, the electrons may return to the original state in the valence band (step 2) or become trapped in the band gap (step 3). For some traps, the repopulation is accompanied by luminescence even during irradiation.

In TLD, the material is evaluated some time (hours to years) after irradiation. Trapped electrons are re-excited to the conduction band by absorbing energy from external heat (step 4). Their return to the luminescence centres is detected by measuring the light emitted during the heating process (step 5). A light output increasing with temperature is initially observed as more re-excitations occur. Traps become gradually empty and the light yield starts to decrease. The glow curve is therefore peak-shaped, and the light output in the TL peak is measured to derive the dose received by the TLD. Various peaks may appear in the glow curve, linked to different defects, and some are only populated by energies of high LET – leading to different glow curves for photon or neutron irradiations. After measurement traps became essentially empty and the TLD can be re-used, in principle.

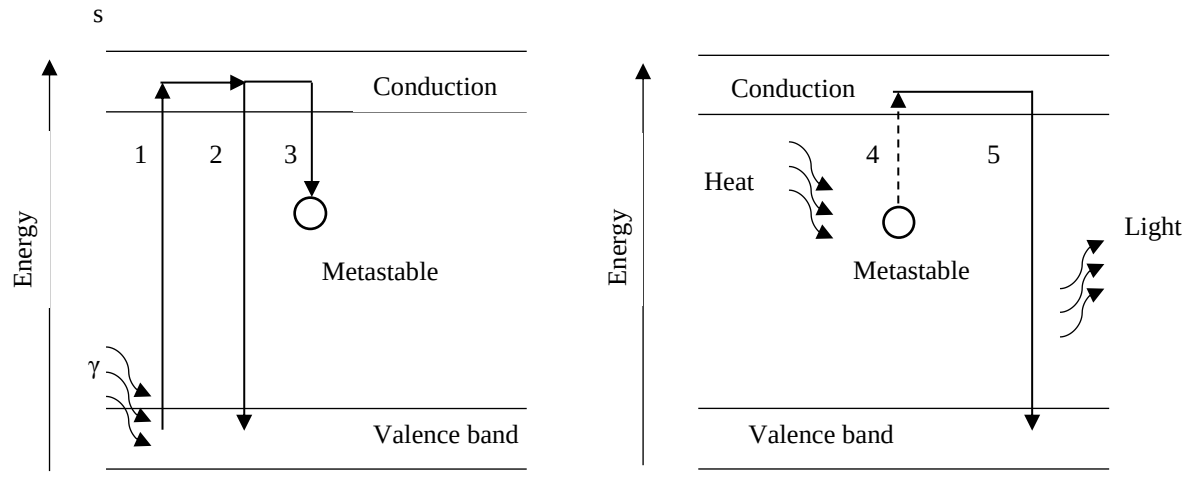

Figure 2-6 Band representation of the TLD during irradiation (left) and during heating (right)

The most popular TL materials commercially available are LiF, LiB_4O_7, CaF_2, $CaSO_4$ and Al_2O_3. TLDs are inexpensive and presented in various forms such as cubic, cylindrical, or raw powder for custom use. Their common use is found in environmental and individual dosimetry. For low-dose neutron applications, the materials may be enriched in isotopes of high capture cross section (^{6}Li, ^{10}B). For reactor dosimetry, high neutron fluences are generally involved and most materials become damaged following neutron exposure. Perhaps the most interesting application of TLDs in reactors is for the discrimination of the photon dose in the mixed radiation field.

In this case, materials of low neutron sensitivity (depleted in ^{6}Li and ^{10}B or based in Al) are used. Their response is normally corrected by the relative neutron sensitivity, determined experimentally.

The TL process is very complex, and for that reason physical models relating the light output with the dose are not very accurate. Instead of applying a theoretical formulation, TLDs are simply irradiated in a reference radiation beam (with a known dose of photons or neutrons) to derive their sensitivity (calibration factor).

3 Materials and methods

3.1 The Portuguese Research Reactor

The RPI operates in the Campus Tecnológico e Nuclear (CTN) of Instituto Superior Técnico (IST). The RPI was acquired from the USA in 1956 in the context of the programme Atoms for Peace, and reached criticality in 1961. It is an open pool reactor, moderated and cooled by light water and using (Oliveira, 2005). In 2007 the core was converted from High Enriched Uranium (~93% ^{235}U) to Low Enriched Uranium (~20%) with the assistance of the Reduced Enrichment for Research and Test Reactors program. Fuel elements are of Material Testing Reactor (MTR) type. Standard fuel elements contain eighteen U_3Si-Al plates (each plate containing 21g of ^{235}U) sandwiched in AG3NE alloy as cladding material. Control fuel elements contain 10 plates and a central cavity for the insertion of the control rod.

The fuel elements are distributed in a grid of 6x9 positions. The core configuration involved in this work employs 8 standard and 5 control fuel elements, and includes Beryllium reflectors. Neutron start-up sources and instrumentation elements are also commutable within the grid. Several irradiation facilities are included (Figure 3-1):

- A thermal neutron column with horizontal and vertical accesses based on a graphite pile that moderates neutrons, having horizontal(A1) and vertical accesses (A2);
- Various beam tubes that transmit neutrons through the reactor walls to external ports (B, C);
- In-core devices for sample irradiations in the core grid (D);
- Gamma irradiation dry chambers (E).

The RPI can reach up to 1MW thermal power. The primary cooling circuit can work until 50ºC. Passive convection cooling is possible up to 100kW (Oliveira, 2005). The neutron fluence rate is directly linked with the power. Three types of instrumentation are used for power monitoring: (i) fission chambers measure directly the neutron output at fixed positions in the core; (ii) thermal probes measure the temperature of the primary cooling circuit; (iii) a closed ionisation chamber that counts mainly the ^{16}N activity in the primary cooling circuit, originated by the $^{16}O(n,p)^{16}N$ reaction (Castro, 2009).

3.2 Cell irradiation experiments

The thermal column (Figure 3-2) contains a pyramidal stacking of graphite blocks inside the reactor pool, between the core and the reactor wall (thermal column extension) and an external pile. A Lead shield of 24cm thickness is placed between the core and the thermal column extension to shield against photons. The vertical access of the thermal column consists of a 1m-diameter well that allows to reach the top surface of the external pile. Some graphite blocks were rearranged and a Lead filter was added to form a cavity at the bottom of the well (2 metres deep) that is very convenient for thermal neutron irradiation of monolayer cell cultures with a reduced photon background. At 1MW, nominal fluence rates at the centre of the cavity are $\phi_0=6.6x10^7$ $ncm^{-2}.s^{-1}$ and $\theta=2.4x10^4$ $ncm^{-2}.s^{-1}$, respectively. The radiation field is uniform along the transversal direction x but the fluence rates decrease with the distance from the core (longitudinal direction y).

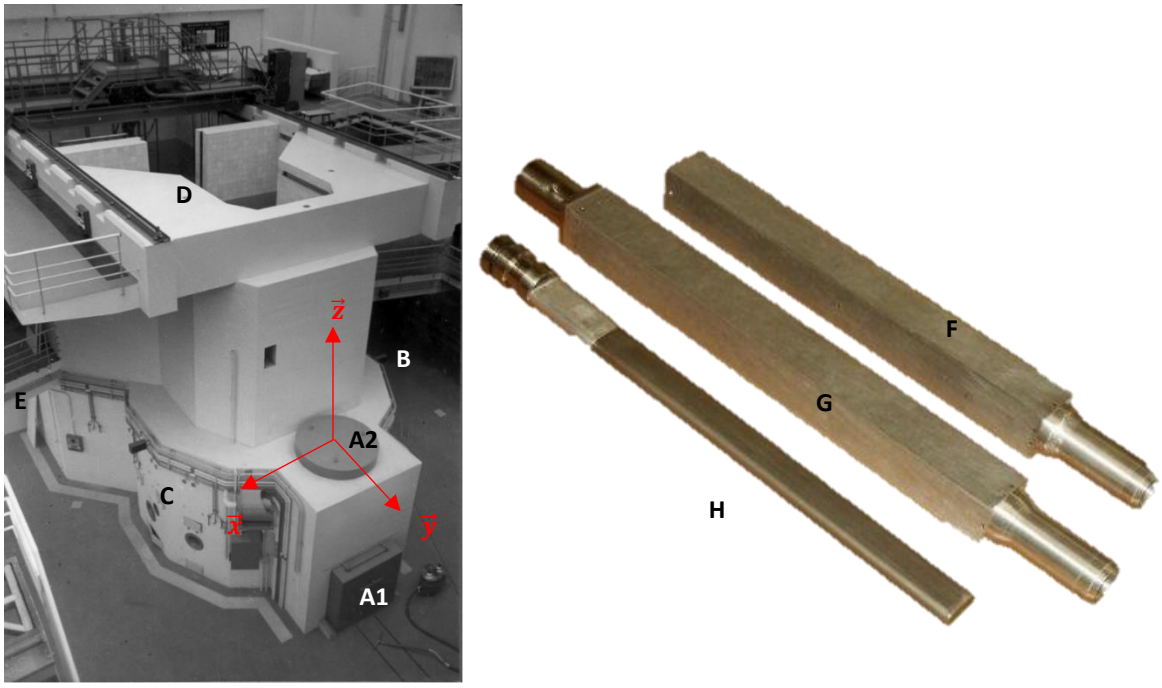

Figure 3-1 General view of the RPI prior commissioning in 1960 (left). Fuel elements (F), with regulation well (G), and moderation rod (H) (right)

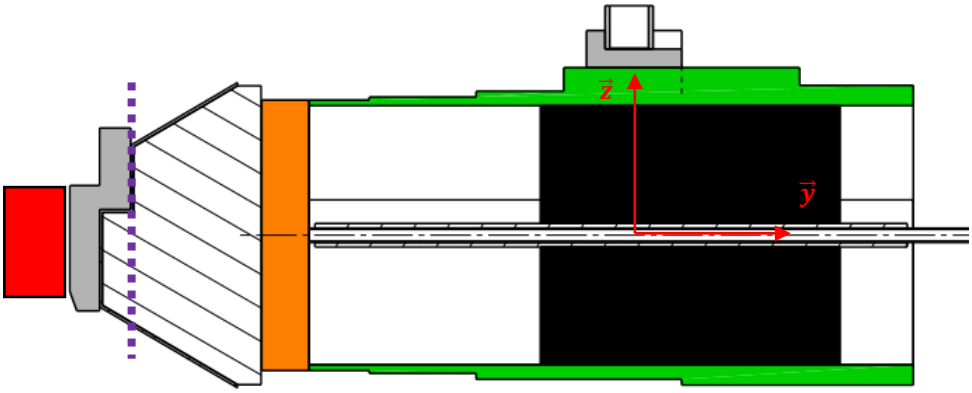

Figure 3-2 Cut view of the thermal column. The core is represented in red. The source file of the core model is applied on the purple line.

GBM cells, of the U87 cell line, were cultivated and incubated with 3 new generation compounds in order to be assessed for BNC cytotoxic effects. The cells were incubated for 30 minutes at concentrations ranging from 50 to 200µM with carboranylmethylbenzoacridone (CMA) compounds before the irradiations.

A cell mono-layer is placed in a flat-surfaced polystyrene culture flask over an area of 25cm^2. The flask is filled with culture medium up to 2mm high; a charcoal filter stopper ensures the air flow and prevents any external contamination. The evaluation of each compound at a certain concentration comprises 4 flasks with cells: a flask with B-loaded cells to be irradiated; a control flask with non-loaded cells to be irradiated (this flask allows to discriminate the effect of BNC over the other radiations); another control flask with B-loaded cells that will not be irradiated (to account for any cytotoxicity of the compound); a blank with non-loaded and non-irradiated cells (that accounts for any effect induced by the cell cultivation and storage in the flask).

For irradiation, the flasks are distributed in a Plexiglas box (thickness of 5mm at the base and 20mm at the side walls) that is placed at a fixed position over the Lead shield in the thermal column. The box allows the simultaneous irradiation of 2 transversal rows of 6 flasks each (Figure 3-3). In general, all flasks are irradiated in the same row (the one closer to reactor core), to be exposed to the same radiation field. Irradiation times ranged from 2h to 4.5h at a nominal reactor power of 600kW.

The base of the irradiation box contains small cavities (one at each corner and one at the centre) in which one gold foil is placed in order to monitor the neutron fluence during each irradiation.

The radiotoxicity of the irradiations as well as the cytotoxicity of the compounds were assessed after irradiation. Early and late damages were quantified by the mean of Double Strand Breaks (DSB) and Micronucleus (MN) assays (section 4.6.3).

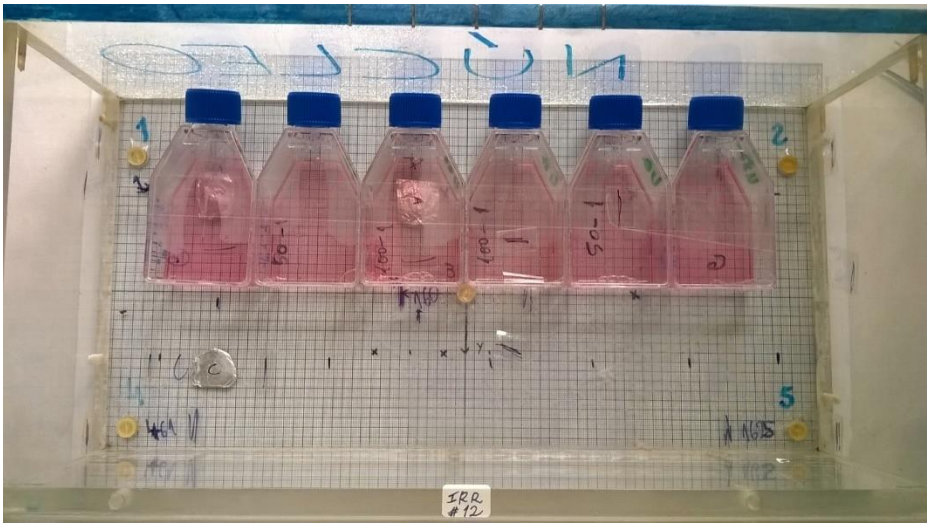

Figure 3-3 A typical set-up for cell irradiation. Note the gold monitors and other detector sets.

3.3 MCNPX characterization of the irradiation facility

A detailed study of the radiation fields at the vertical access of the thermal column was performed to interpret the foil measurements (by including the perturbation in the neutron field potentially induced by the samples) and address the contamination of the thermal neutron field by gamma rays, epithermal and fast neutrons.

The code used during this assay is MCNPX version 6.1, developed and released by Los Alamos National Laboratory, USA. This code allows for fixed-source simulations (of various particle types) and neutronics studies. In this work, the existing core model was used to extract the source term for the subsequent simulation of the thermal column. The source term consisted of a file in which the positions and velocities of 40.7 million neutrons crossing a surface at 25cm from the core (Figure 3-2) were stored.

3.3.1 Geometry and materials

The geometry of the Monte-Carlo model is mainly defined by surfaces, with cells being defined by intersections, unions and complements of regions bounded by the surfaces. MCNPX also allows for microbodies, but these were avoided to increase the calculation performance of the system. A computer-aided design (CAD) model of the facility's geometry was built (annex 0) and exported to the input file of MCNPX. Actual dimensions were measured during previous works or extracted from existing blueprints. The nomenclature included in the

latter indicated the nominal composition of the construction materials, such as steel type, barite-loading of concrete or aluminium series. The graphite density was measured on an original spare block and a Boron-equivalent contamination up to 10ppm was allowed (OEEC-NEA, 1959) to include any unaccounted neutron-absorbing impurities.

3.3.2 Tallies

The energy distributions (spectra) of neutron and photon fluences and photon energy fluence were calculated at the surface of the empty irradiation box: the target volume consisted of a 1mm-thick air slab of 602 cm^2 adjacent to the box surface. Dose calculations were based on flux-to-dose-rate conversion factors: kerma factors for neutrons and mass absorption coefficients for photons. Because the experiments deal with biological samples, doses were calculated in the air that constitutes the target volume and in water (the main ingredient of tissue). In the latter case, doses were also derived directly from the calculated energy deposited in the target volume filled with water. Finally, the number of neutrons crossing the surface of the irradiation box was simulated to extract their angular distribution. In summary, the following MCNPX tallies were used:

- Neutron fluence rate (F4 tally: fluence averaged over a cell);
- Modified neutron fluence rate (FM4 tally, modified with the flux-to-dose conversion factors to yield the dose);
- Neutron energy deposition (F6 tally: energy deposition averaged over a cell);
- Photon fluence rate (F4);
- Modified photon energy fluence rate (*FM4 tally);
- Photon energy deposition (F6);
- Neutron angular distribution (F1: current integrated over a surface).

The energy bins for the F4 and F6 tallies were extracted from the BUGLE-47 group structure (47 neutron and 20 photon). The first neutron energy bin (0 – 0.468 eV) includes the whole thermal region, and has been therefore sub-divided in 38 bins to retrieve the detailed spectrum in this region. The angular distribution was retrieved in only 3 energy groups corresponding to the thermal (<0.5eV), epithermal (0.5eV-100keV) and fast (>100keV) regions.

The target volume was divided in 4 equi-width transversal strips to obtain the longitudinal distribution of the neutron and photon fluences with respect to the distance from the reactor core.

3.3.3 Variance reduction

The large distance and vertical displacement of the irradiation cavity relative to the core and the vast graphite pile render the Monte Carlo simulation difficult due to the reduced fraction of source neutrons that reach the target volume. Variance reduction techniques were necessary to achieve a good statistical uncertainty and reduce calculation time. MCNPX embeds several variance reductions technics to decrease the computation time, those used in this work were:

- Cutoffs in time, energy or geometry. Particles crossing a defined area or reaching a low energy are not tracked anymore as they are not significant for our results. The cutoffs used in our case were mainly

geometrical: neutron transport beyond the external graphite pile and across some regions displaced vertically from the surface source and far from the irradiation box was not considered;

- Geometry splitting reduces the efforts to track particles in cells defined in the geometry model that do not affect the result significantly (typically, cells far from the target volume). A Russian Roulette algorithm selects the unimportant particles to kill, but increases the statistical weight of the surviving ones. In interesting places, particles are divided in two or more, but are given a lower statistical weight. More tracks can therefore be followed for a constant overall statistical weight.
  For each cell, an importance parameter is attributed. If a particle of weight W crosses a cell of importance i to another cell of higher importance j, the incoming particle is divided into n particles of weight W/n with n=j/I, if n is not an integer, the cell is divided randomly. It is recommended that the importance ratio between adjacent cells is smaller than 4;
- Mesh Weight Windows (WW) are powerful means of variance reduction in MCNPX, based on geometry splitting over a mesh that is superimposed to the model without requiring a sub-division of the geometry. An input card manages the importance of particles on energy. When the particle crosses the virtual window, its weight determines its future. If the weight is smaller than the lowest weight bound WL, Russian roulette is applied; if it survives, a superior weight is attributed. If the weight is higher than the upper weight bound WU, it is split in several particles of lower weights. If the weight is between the two bounds, no modification is operated.

MCNPX contains a WW generator that determines WL according to the neutron population of each mesh during a run. In this work the generator was used to obtain initial values for the WW that were tuned manually to attain a progressive weight increase (ratio<4) from the core to the cavity (Figure 4-1).

3.3.4 Normalization and coupling to core model

MCNPX outputs are relative to one source neutron. To scale the results to the emission rate of fission neutrons, a normalization factor F is applied:

$$F = n_f \times \frac{\bar{\bar{\upsilon}}}{k_{eff}} \times P \qquad \text{(eq.34)}$$

where $\bar{\upsilon}$ is the average number of neutrons emitted per fission, k_{eff} is the effective multiplication factor and P is the reactor power in watt. The number of fissions per watt-second n_f is:

$$n_f = \frac{1 joule/sec}{watt} \frac{1 MeV}{1.602E-13 joules} \frac{fission}{198 MeV} \approx 3.15E10\ fission/watt-sec \qquad \text{(eq.35)}$$

The values of $\bar{\upsilon}$ (2.42) and k_{eff} (0.99) are extracted from the core model. The recoverable fission energy is known to depend mostly on the core materials (fuel, clad, coolant, reflector) and on the fuel burnup. For the fission of ^{235}U, values can vary from 198 to 207 MeV/fission (Sterbentz, 2013) (Los Alamos, 1997). The lower value was adopted, as it leads to a good agreement between the calculated and measured neutron fluence rates using the RPI core model (Fernandes et al., 2010).

3.4 Neutron fluence rate measurements

3.4.1 Activation foils

The radiation field at the base of the irradiation box was characterised with Gold foils for thermal and epithermal fluence rate measurements by the Cadmium-ratio method. Circular foils of 100% Au with dimensions (Ø6mm x 50µm) and weighting about 30mg each were used. The activation reaction $^{197}Au(n,\gamma)^{198}Au$ was considered. Important data for this reaction is: a=100.00%; M=196.9665; $T_{1/2}$=2.696day; E_γ=411.8044keV; p_γ=95.56%; σ_0=98.65b; I=1550b; g=1.0051 (NEA, 2016).

Figure 3-4 Gold detectors and its cadmium cover used for epithermal neutron fluence rate measurements

Foils are handled with gloves and tweezers to avoid contamination and can be cleaned with alcohol if necessary. The foils and the foil-containing Cd filters are wrapped in a thin aluminium foil and attached to the box surface using scotch tape. In the special case of the monitors in the corners, the foils are simply introduced in small plastic holders and covered with scotch tape (Figure 3-3).

Foil activities were measured in a gamma spectroscopy system using a High-purity Germanium crystal (HPGe) Camberra GC-2018. The germanium crystal is a semiconductor having a sandwiched structure of negative, depleted, and positive layers. An electric field is applied between the electrodes, and photons interact with the depleted layer.

Holes and electrons are produced inside the crystal and the charge generated is proportional to the energy deposited by the photon. The charge is detected, amplified and directed to a 16384-channel multi-channel analyser (MCA). The value of t_m was adjusted to accumulate at least ~10000 counts in the 411keV peak, corresponding to 1% statistical uncertainty in the activity measurement. It was checked that dead times were below 7% in order ensure the application of accurate dead-time corrections retrieved by the software.

3.4.2 HPGE efficiency

The system was calibrated for energy and efficiency using a set of standard pointwise photon sources of know activity at a reference data (annex 0). Source activities were corrected for the decay between the reference and measurement time. Efficiency points $\eta(E_\gamma)$ were measured and fit to a polynomial curve in a log-log scale.

The efficiency depends on the crystal-to-source distance. A reference distance of 14.5cm was used for calibration. Occasionally, it was necessary to attain higher efficiency by reducing the distance to 1cm. The foil can no longer be considered pointwise, and an efficiency conversion was made by measuring at both distances a similar, activated Au foil with the same geometry. The uncertainty in each response measurement is estimated by error propagation, with a dominant contribution from the uncertainty in the source activity (1-2%). An overall uncertainty of 2% can also be derived from a participation in a round-robin exercise on foil activity measurements (institution 4 in (Thornton et al, 2016)).

An attempt was made to detect fast neutrons using an Indium detector via inelastic scattering in ^{115}In, but no activity was detected (even with a NaI scintillator, having a higher efficiency than HPGe).

3.5 Photon dosimetry

Photon doses were measured with TLDs of Al_2O_3:C and ^{7}LiF:Cu,P,Mg provided by Thermo Fisher Scientific under the designations of TLD-500 and TLD-700H, respectively. Dosemeter dimensions are ∅4.5x0.8mm (TLD-500) and 3.2x3.2x0.3mm (TLD-700H). These materials were selected for their low sensitivity to thermal neutrons. The measured relative thermal neutron sensitivity for TLD-500 ranged from 3.5 to 4.0. The thermal neutron sensitivity of TLD-700H has been reported as 3-10 smaller than that of ^{7}LiF:Mg,Ti - a popular TLD similar to TLD-700H but with different dopants, for which 18mGy ^{60}Co/10^{10} $n_{th}cm^{-2}$ has been measured. The data are consistent with the application of a common value for the relative thermal neutron sensitivity of both materials, assumed as 3.5mGy ^{60}Co/10^{10} $n_{th}cm^{-2}$.

The TLDs were calibrated individually for kerma in air using a ^{60}Co source at the metrology laboratory of IST/CTN. The calibration was performed with 100mGy, with a field size of (14.4 x 14.4)cm at 1 meter from the source corresponding to an air kerma rate of 750 μGy.s^{-1} and 850 μGy.s^{-1} of dose in water. A set of 31 TLDs was irradiated simultaneously in an opaque Plexiglas support of 5 mm thickness (Figure 3-5).

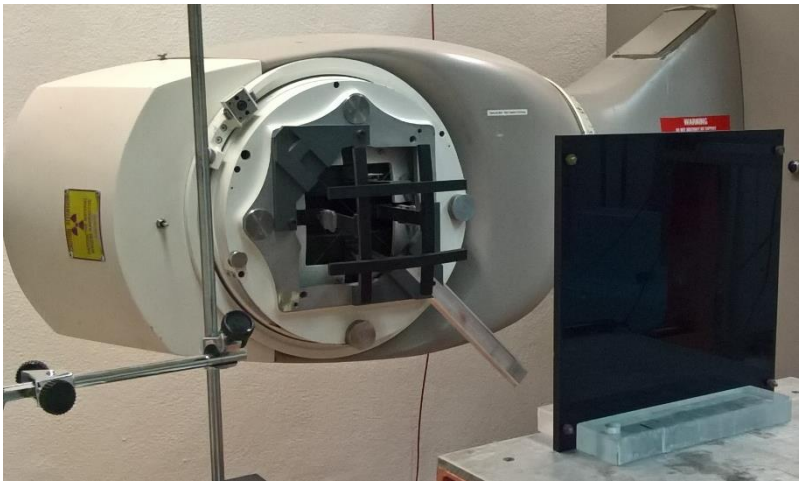

Figure 3-5 A 60Co irradiator used to calibrate a set of 31 TLD in their linear response curve

The TLDs were evaluated in a Harshaw 3500 reader (Figure 3-6). Resistive heating is transmitted to the TLD holder in a readout chamber flushed with N_2 at a flow rate of 1L.min^{-1} (flushing allows to eliminate oxygen-related signals such as combustion). The heating is performed at 5ºC.s^{-1} up to a maximum temperature of 350ºC (TLD-500) and 240ºC (TLD-700H). The glow curve is integrated between 100-260ºC (TLD-500) and 140-230ºC (TLD-700H).

Care is taken to irradiate and keep the dosemeters protected from ultra-violet light because it can re-excite the trapped electrons thereby inducing an appreciable signal loss (fading) in TLD-500. In general, a small time-dependent fading occurs due to the spontaneous return of electrons to the valence band. This effect is more pronounced on the first hours following irradiation. To reduce its influence, the TLDs were always readout 24h after irradiation.

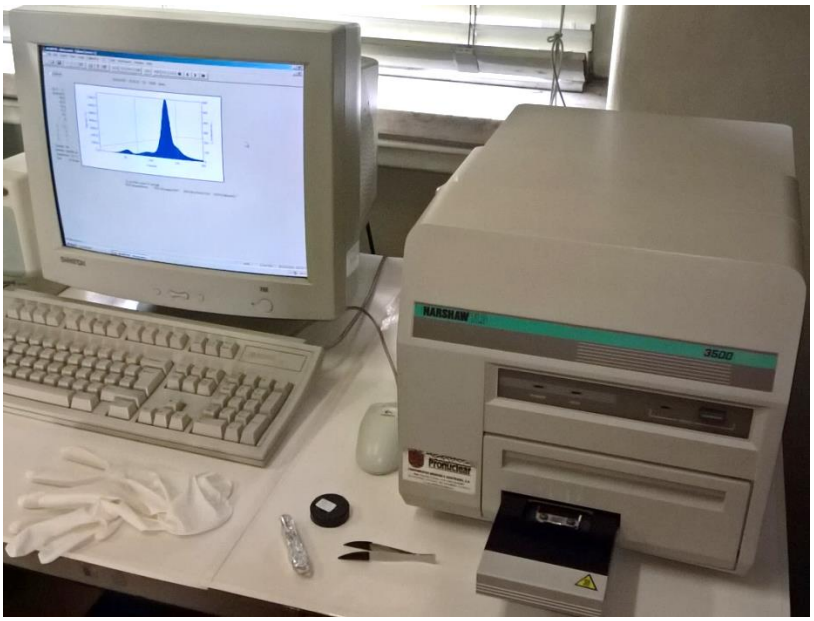

Figure 3-6 A computer-operated TLD reader used during this work (Harshaw 3500)

In each measurement point a pair of TLDs was employed, one of each material. The TLDs were inserted in a small, light-tight paper pack and attached to the box surface. Prior to irradiation, the residual signal is erased and the sensitivity is restored by a thermal annealing process. TLD-500 is annealed for 1h at 600ºC followed by slow cooling over more than 12h. TLD-700H loses sensitivity when subject to temperatures above 240ºC. This material is annealed at 240ºC for 12s in the reader and readout twice.

The reader can suffer small sensitivity fluctuations due to, e.g., temperature, and varying TLD sensitivities may also be induced during the annealing process. Control dosemeters are employed to correct for any fluctuation. These consisted of 5 TLDs (for each material) that were exposed to electrons in a ^{90}Sr/Y irradiator. Control TLDs are readout and annealed together with the "measurement" TLDs, but are always subject to the same exposure conditions at the irradiator. In this work, a ^{60}Co-equivalent dose of 100mGy was given.

3.6 GEANT4 model of the experience

GEANT4 is a particle transport simulation code developed initially by the CERN for high energy physics. After years of development, it became a reference in the physics simulations with applications for personal dosimetry, space exploration, nuclear medicine (Agostinelli et al, 2003) (Allison, 2006). Its high precision libraries allow to simulate and analyse also the interactions generated by low energy neutrons. The ability to track primary and secondary particles, as well a high customization potential made it a good candidate for microdosimetric simulations and furthermore with an eye on the GEANT4-DNA package for future DNA damage simulation (Bernal et al., 2015).

The GEANT4 models will estimate the following:

- The dose repartition in the cell layer, sorted by particle type;
- The dose received by a cell in a bidimensional cluster;
- The dose received by each part of a cell.

Different simulations will be designed: a global geometry of the experiment (3.6.1) and a cluster cell model (3.6.2).

3.6.1 Global geometry model

The simulation aims to quantify the collaboration of each kind of primary particles (neutrons and photons), and secondary particles (protons, alphas, electrons, photons from capture reactions and scattered nuclei) to the overall energy deposited in the cell culture volume within the flask.

The model comprised the irradiation cavity with the Lead filter, irradiation box, culture flask and chemical compounds (Figure 3-7).

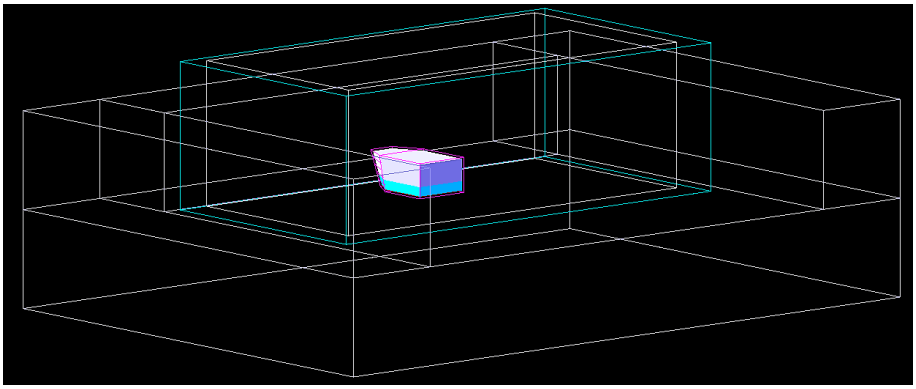

Figure 3-7 Geometry of the GEANT4 global geometry model for dose repartition.

Not all the thermal column was assessed as the previous MCNPX model already considered the moderation, scattering and attenuation occurring in its geometry. MCNPX results in the absence of the irradiation box, namely neutron and photon spectra and fluence rates, were input on the top surface of the lead shield, coupling the two simulations.

The flask used for cell culture is made of polystyrene (1mm thick) for its excellent optical characteristics, required for fluoroscopy analysis. The flask was placed along the longitudinal axis of the experience chamber, at 2cm from the wall of irradiation box closest to the reactor core.

A single cell layer grows attached to the bottom of the flask. The cell layer was constructed as a 200µm high by 25cm^2 (0.5mL) volume. Knowing the confluency of the cell culture from previous visual observations, it has been considered that the cell layer simulated is composed of 20% water and 80% brain cells - having the same elemental composition as the brain from ICRU reports (Table 3-1). A concentration of natural boron was set to 25ppm, a value corresponding to a CMA concentration of 230 µM. The homogenous liquid cell layer weighted 0.5132 grams.

Table 3-1 Elemental fraction input for the cells simulated, from ICRU report 44, brain composition.

Element	*H*	*C*	*N*	*O*	*Na*	*P*	*S*	*Cl*	*K*
Mass fraction	0.107	0.145	0.022	0.712	0.002	0.004	0.002	0.003	0.003

The growing medium, mostly made of water and nutrients, covers the cells up to 2mm high. This layer affects in principle the radiation field and was therefore included in the model.

Because of the small thickness of the cell culture, few interactions are expected and consequent calculation time may be required to obtain results with good statistics, two variance reduction technics were employed:

- A general increase of all the cross sections by a factor of 10 was set up following the «BiasCrossSectionByFactor» method.
- A factor of 10 was applied to the virtual composition of the cell layer with respect to the admitted concentration.

Neutrons were generated in three energy groups: thermal, epithermal and fast, each having the energy and angular distributions extracted from the MCNPX model. This discrimination helped determining the interactions and deposited energy provoked by each energy group. For scaling, it was considered that fast, epithermal and thermal neutrons compose respectively 0.11%, 0.21% and 99.67% of the total neutron fluence rate in the thermal column, in accordance to MCNPX results and foil measurements. Photons were simulated with the MCNPX energy distribution and with isotropic emission. The particle emission surface is limited by the Lead shield, with an overall area of 2500cm^2.

3.6.2 Microscopic model

The microdosimetric model of the cell cluster aims to quantify the dose received by the U87 cells incubated with CMA at levels encountered during actual BNC experiments.

Cells were represented in a planar cluster so it is possible to monitor fragments from surrounding cells that may impact a central cell (cross-fire).

A central cell, of dimensions given by the radiobiology laboratory is composed of 2 structures: a cytosol shell and a nucleus sphere. Cytoskeleton, being geometrically located at the same place of the cytosol, is not represented, and its boron content will be attached to the cytosol. The cell membrane of a mammalian cell being in the range of 4nm, was not represented in the microdosimetric model, and any boron content determined experimentally was *in lieu* reported in the cytosol. The 2 cell structures are assumed to have both the elemental composition of brain cells (Table 3-1). The cell cluster contains 15 cells plus a central sensitive cell, where the doses will be assessed. Three runs will take place:

- Dose received by the central cell when all cells have boron;
- Dose received by the central cell when all but the central cells have boron;
- Dose received by the central cell if boron is present in surrounding water.

The repartition of Boron in the cell volumes was determined by Inductively-Coupled Mass Spectrometry (ICP-MS), results being reported in Section 4.6.2. The model included an average cell uptake of 237ppm ^{10}B. This value corresponds to the upper limit obtained with a 350µM concentration of CMA. During real irradiations, a

lower concentration (50 to 200µM) was used, presumably below detection limits of ICP-MS. This 237ppm will act as an upper limit for dose estimation.

To decrease computation time, only thermal neutrons will be generated from a planar source, as previous simulation showed that epithermal, fast neutrons and photons had a very low impact on the overall dose.

3.7 BNC experiments

3.7.1 Cell culture

U87 malignant glioblatoma is a type IV astrocytoma cell. The cells were grown during 24 hours in a growing medium (DMEM+Glutamax I) supplemented with fetal bovine serum and penicillin/streptomin. The cultures were maintained at 37ºC in a 5% CO_2 humidified atmosphere. The cells were seeded in culture flasks (10^6 cells) and occasionally in microplate wells (about 200µL, 10^4 cells) for the assays. Prior to irradiation, cells were incubated for 30 minutes with various concentrations of CMA (Figure 3-8).

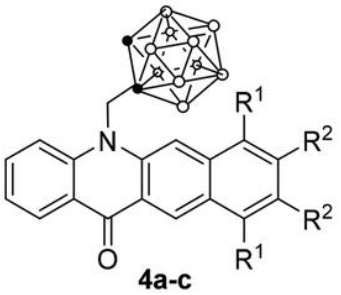

Figure 3-8 The boron compound family, carboranylmethylbenzoacridone used in this study.

3.7.2 Cytotoxicity evaluation of CMA by MTT assay

The cytotoxicity of the boronated compound (CMA) was evaluated by the MTT assay. The MTT is a tetrazolium compound that can enter the cells and be reduced by oxidoreductase enzymes in the mitochondria. This assay measures the metabolic activity of the living cells which can be correlated with the number of cells. Two independent experiments were conducted for the cytotoxicity assay in 96 well plates, each one consisting of six concentrations of the boronated compound, six replicates each and compared with the controls (no treatment). Control cells was considered 100% cellular viability, and the cellular viability of incubated cultures was calculated in relation to controls. For the MTT assay estimating the cytotoxicity of the compounds prior irradiations, CMA was incubated with the cells at different concentration, ranging from 0 to 200 µM. After 6h of incubation, the growing medium was discarded and a solution of MTT in PBS (0.5mg/mL) was added to the cell cultures. After 4h the MTT was removed and the crystals of reduced MTT (formazan) were dissolved in DMSO. The absorbance in each well was determined by a plate spectrophotometer.

After irradiations, the radiocytotoxic effect were evaluated by the same method.

3.7.3 Analysis by ICP-MS

ICP-MS allows the detection of traces of numerous elements in a fast and accurate way with the possibility to detect elemental levels low as ppb. In an ICP-MS equipment, the sample, in liquid state is often dissolved in

hot nitric acid. The sample fluid is nebulized with argon by Venturi effect. The torch itself is heated by induction (high frequency alternative current), were an argon flow is turned into a neutral plasma at around 6 000K. The concentric geometry of the torch allows a central pipe to be inserted, where our sample will be ionized. At the end of the ICP, a set of metallic slabs acts as an electrical lens, focusing the plasma. The sample plasma converges on a quadrupole, that acts as a mass filter. The mass filter, sorts the incoming ions by their ration m/z, it is coupled with a dynode and sends the pulses to a computer. The quadrupole fluctuates its m/z ratio electrically, and any ion passing the filter will be recorded by the dynode. During the ICP-MS measurements, attention was paid to avoid any contact with glassware, containing Boron that may be dissolved by the nitric acid. A special plastic container, resistant to heat and acid was used, and several signal calibrations were performed prior and during the measures. A calibration sample, containing several low masses elements at ppm levels was run several times prior and during the cells measurements to prevent any drift in the ICP-MS results.

The cell cultures were incubated with 3 tested boronated compounds one hour with a dose deliberately higher than during the irradiations for detection limit reason. The cells were then counted and decomposed in their respective membrane, cytosol, cytoskeleton and nucleus. The ICP-MS of these fragments allows to estimate the content of boron in the different compartment of the cells, and the total cellular uptake.

3.7.4 Radiation effects

The radiation effects induced by the BNC reaction were evaluated by the radiocytotoxic effect using the MTT assay for viability of the cell culture quantifying, and biomarkers of radiation effects.

Radiation effects were sorted in two categories, early and late damages. For early damages, the Double Strand Break (DSB) evaluation by the mean of γH2AX gene assay was applied, while the micronucleus assays characterised late damages.

γH2AX is a gene used in radiobiology for Double Strand Break (DBB) assays. The double strand breaks are a good estimator for early damages provoked by particles in the DNA that cannot be repaired. Red dots indicate an accumulation of γH2AX, and so of a DSB. The procedure of γH2AX assay was the following: after irradiation, the cells were washed in a 4% PBS solution, then fixed with a formaldehyde solution at 4% during 15 minutes. The formaldehyde was removed following another wash by PBS. To permeabilise the cells, a 0.5% Triton X100 solution was left incubated for 5 minutes. The cells cultures were washed and blocked by a 4% BSA solution during 1h. The γH2AX antibody could finally be incubated at a dose of 2µg/mL during 2h. At the end of the lapse, a double wash by BSA at 1% was applied, and a fluorescent stain (Hoechst) was incubated at 1ug/mL during 5 minutes. Pictures were taken with a fluorescence microscope to estimate qualitatively the DSB occurrences.

Micronucleus counting is a common test for late damages induced by radiations or chemicals. During the mitosis of the cell, a 3rd nucleus, usually smaller and uncomplete may appear if chromosomes are missing or damaged (Figure 3-9). The micronucleus occurrence in the irradiated and control flasks were counted 72h after irradiation.

The cytokinesis process was inhibited by adding 2mg/mL of cytochalasin B. To enlarge the cells and simplify the visual checking for micronucleus, a hypotonic shock was applied to the culture, previously centrifuged.

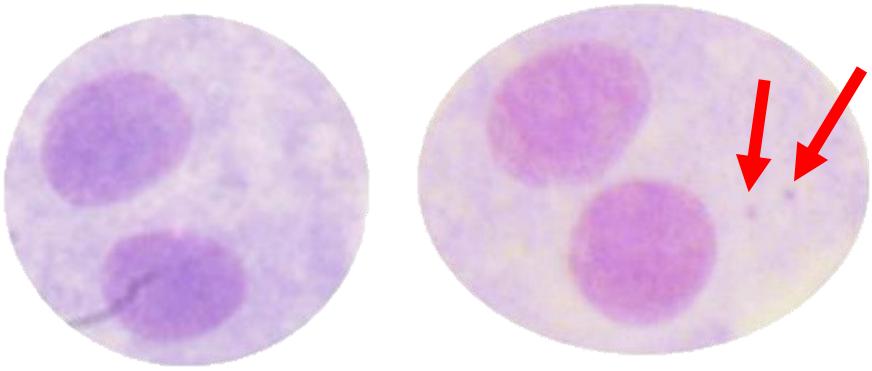

Figure 3-9 Micronuclei pictures, left is a normal division, right shows 2 micronucleus (arrows).

Fluoroscopy is a good indicator for the relative distribution of the compounds inside the cells. The compound injected was traced with a fluorescent stain to allow visualisation of the intake inside the cell. Only the nucleus and the cytosol/cytoskeleton regions were distinguishable. Because only a small percentage (typically less than a percent) of the compound enters the cells, the medium had to be washed in PBS several times to remove any background fluorescent signal.

4 Results and discussion

4.1 MCNPX simulations

Three input files were necessary for the MCNPX simulation of the radiation field at the surface of the irradiation box: (i) description of the geometry, materials and tallies; (ii) mesh-based WWs for variance reduction, and (iii) surface neutron source from a criticality run of the RPI core model. Simulations were made on a 64GB, 32-core computer at IST/CTN. Each run took 2.6 days to complete the simulation including photons. Figure 4-1 shows the geometrical model together with the variance reduction mesh and the incidence of collisions in each mesh cell. A single mesh was employed along x because the relevant directions of the radiation transport from the core to the thermal column is along y and z. Mesh size along y and z in graphite and Lead is 3.2 cm corresponding to the mean free path of neutrons in these materials. A coarse mesh was considered in air due to the reduced radiation attenuation and at the low graphite region - which receives few source neutrons and is far away contributing little to the radiation in the target volume. Regions beyond the external graphite pile can only contribute through backscattered radiation and were given importance 0 for being too far away. Inside the pool, regions above the core were given reduced importance because they receive few neutrons from the surface source and loose energy very fast displaying a low penetration through the concrete wall.

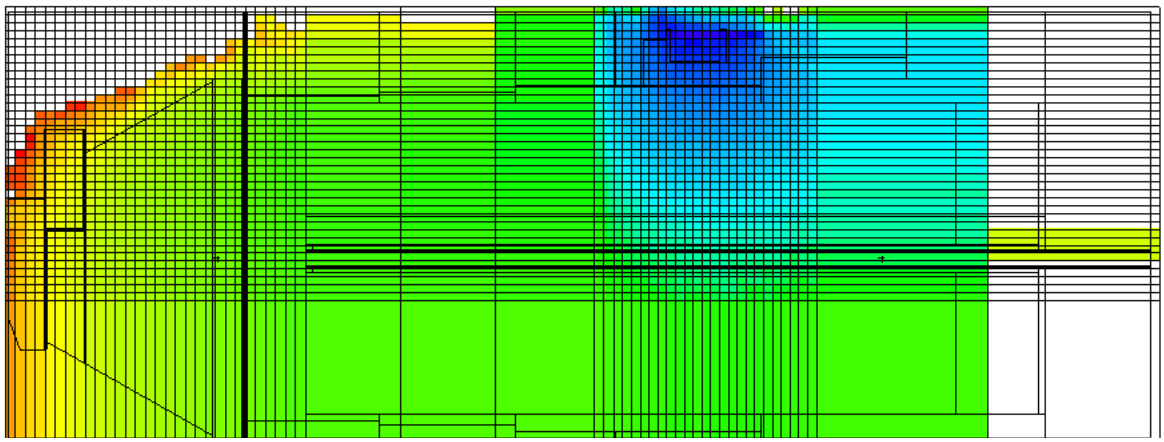

Figure 4-1 MCNPX model of the thermal column (Y-Z cut). The mesh considered for variance reduction is superposed. Red indicates high interaction intensity

The measured graphite density is 1.7g.cm^{-3}, significantly lower than the value considered on previous simulations of the core and thermal column (2.27g.cm^{-3}). Several runs of the MCNPX model of the core were run to estimate the boron contamination of graphite. Figure 4-2 shows that the presence of boron affects significantly the thermal neutron fluence rate, with negligible influence over the epithermal component. After comparisons with neutron fluence measurements (section 4.2.2), a concentration of 10ppm of natural boron was set in the entire graphite pile (~5.5tons). For the comparison, the calculated group fluence rates between 876meV and 10.7eV (covering the 5eV region) were converted to θ.

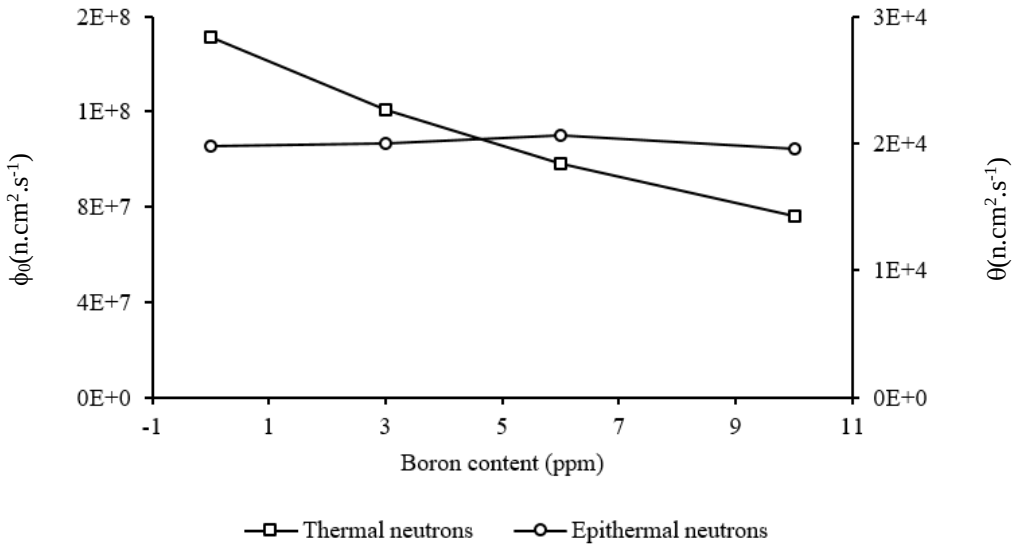

Figure 4-2 Neutron fluence rates obtained under several boron contaminations in the graphite.

The calculated neutron energy spectrum in air (Figure 4-3) shows a clear dominance of thermal neutrons (below 0.5eV) over the total neutron population. Some fast neutrons are expected, as well as an epithermal component almost 10^4 lower than the thermal neutron fluence. The calculated neutron fluence rates at 1MW are: ϕ_{th}=7.59x10^7; θ=1.96x10^4 and ϕ_f=4.82x10^4 (fast neutron fluence rate).

The perturbation induced by the samples on the radiation field was investigated (Figure 4-3). Culture flasks were simulated by 1mm polystyrene with a 2mm layer of 21.6ppm natural boron solution on top. An air gap of 1mm between the irradiation box and the flask was included. There is a global increase of the neutron fluence rates up to 8.48x10^7 (thermal), 2.06x10^4 (epithermal), 5.04x10^4 (fast) due to the neutron reverberation in the hydrogen-containing materials. No significant change in the spectrum temperature appears despite the presence of the absorbing boron layer.

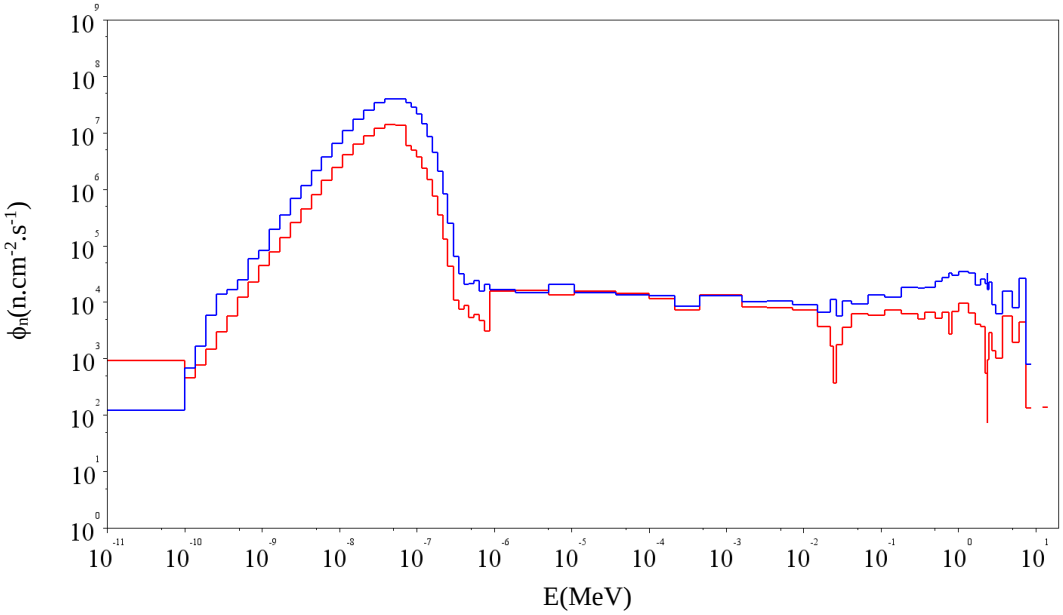

Figure 4-3 MCNP output of the neutron spectrum per unit lethargy in the empty experience box (red) and filled with 2mm of 21.6ppm boron solution (blue), normalized to 1MW reactor power.

With respect to the angular distribution of the neutrons Figure 4-4 shows that most are transmitted across the surface of the irradiation box (positive angles in the figure). Backscattering increases at low neutron energies, being responsible for the maxima observed for thermal and epithermal neutrons. Fast neutrons crossing the surface perpendicularly simply progress without any further collision.

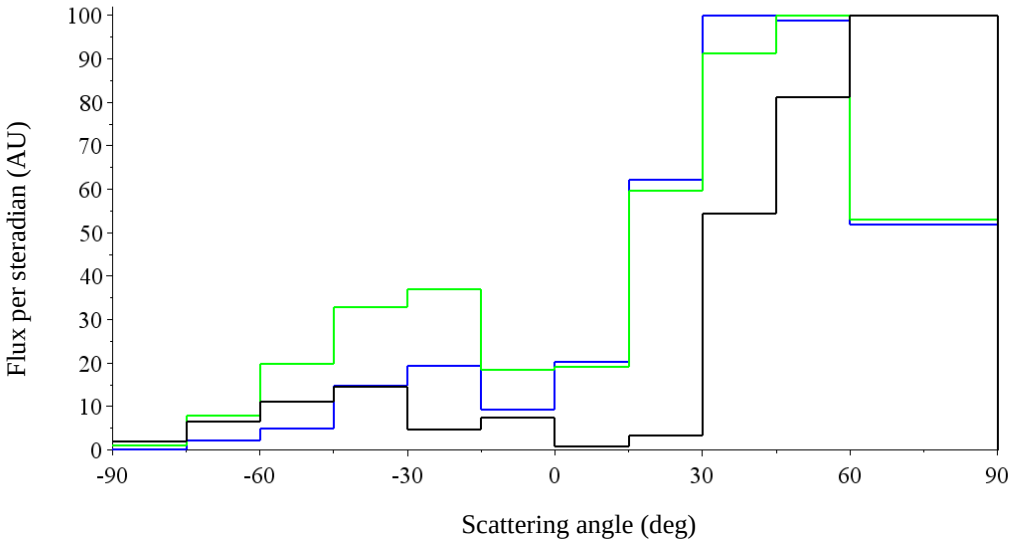

Figure 4-4 Angular distribution of neutrons inside the experience box. Angle is between XY plan and particle track. 0° is at –Z (backscattered perpendicularly to the surface), +90° follows +Y (away from core). Thermal (green), epithermal (black), fast(blue) neutrons are plotted.

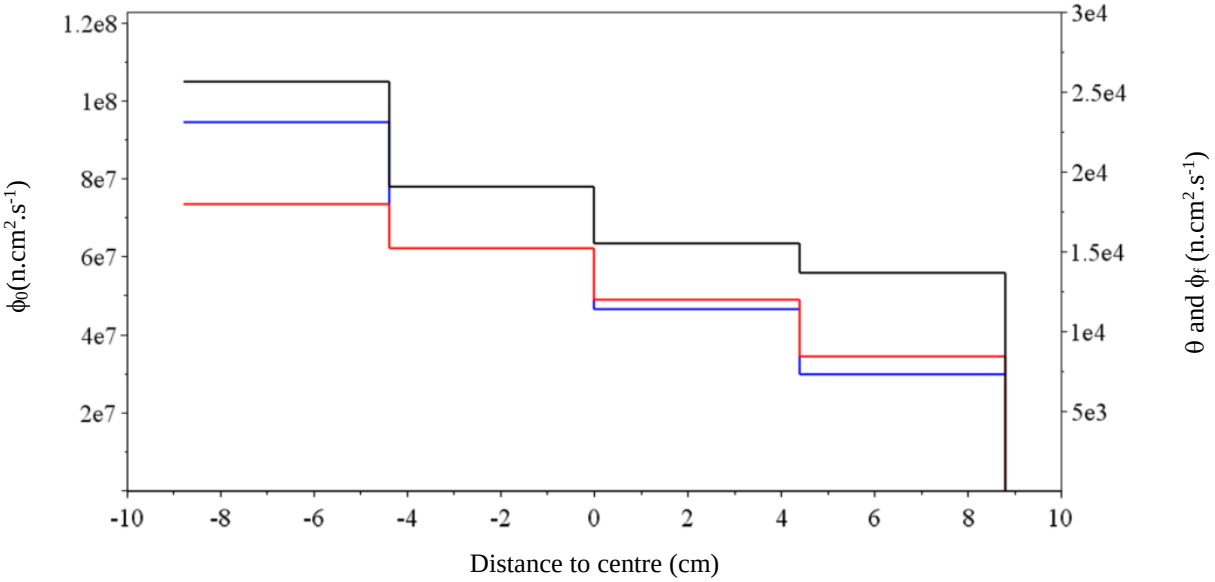

Figure 4-5 Thermal (black), epithermal (blue) and fast (red) neutron fluence rate distribution along the y axis of the irradiation box, normalized to 1MW reactor power.

The distribution of the neutron fluence rate along the y axis (Figure 4-5) shows a clear decrease with the distance from the core. For fast neutrons the evolution is approximately linear with y while for thermal neutrons

an inversely proportional distribution is observed. An average thermal neutron gradient of 5%cm^{-1} (from 10.51 to 5.59)x10^7 $ncm^{-2}s^{-1}$ over 18 cm) is found.

4.1.1 Neutron dose in water

The neutron dose was computed for a 1mm water layer covering the entire irradiation box that simulates the irradiated cell layer. The dose was calculated with a F6 tally, as well as a F4 modified tally that includes the kerma factors in water (Figure 4-6). These were obtained from (Caswell, 1980) above 10eV and derived from elemental values down to 25.3meV.

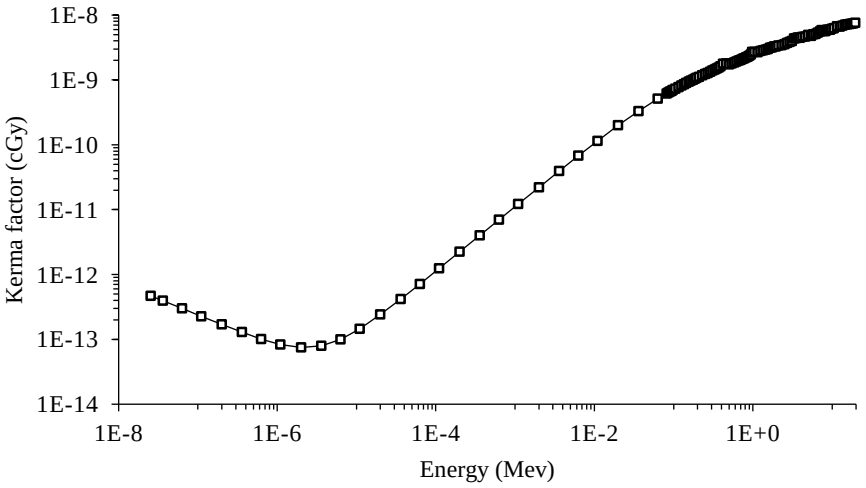

Figure 4-6 Calculated neutron kerma in water (in rad, or cGy) obtained from Caswell 1980.

A GEANT4 model of the water volume was also built to compare its results with the 2 MCNPX approaches. GEANT4 simulations were performed on a personal computer in 3 neutron source energy groups (10^6 particles each) to discriminate the contribution of thermal, epithermal and fast neutrons. The energy distribution in each group is retrieved by the MCNPX model. The results (Table 4-1) show a good agreement among the 3 calculation approaches.

Table 4-1 Comparison of Monte-Carlo simulations of the neutron dose in a 1mm thick water layer.

	D_n *(mGy/h)*	ε *(%)*
*MCNP (*F4)*	8.50	9.46
MCNP (F6)	9.60	8.38
GEANT4	7.54	18.26

The influence of the sample thickness was investigated using GEANT4. For thermal neutrons, most of the dose is due to hydrogen capture. The released 2.2MeV photons travel across the 1mm layer without depositing entirely their energy: electrons above 1022keV are observed as the main contributor to the dose. Fast neutrons mostly transfer their energy by elastic scattering, leading to high velocity protons and nucleus recoils that are

stopped within the layer (thereby originating the high kerma factors at this energy range). As the volume is increased, fast neutrons are thermalized and the gamma rays energies are totally absorbed; thermal neutrons are the main responsible for dose delivery (Figure 4-7).

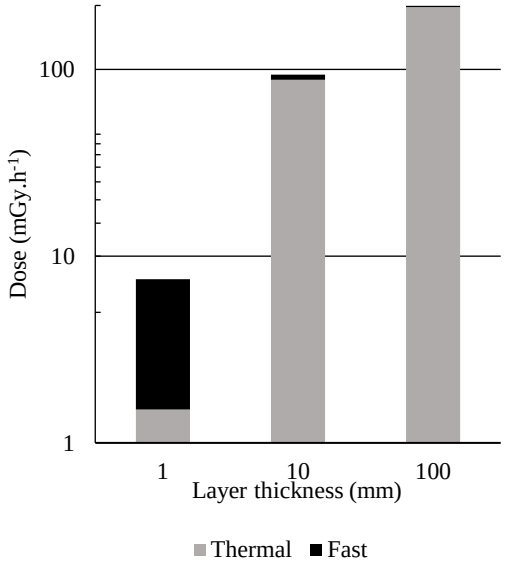

Figure 4-7 Dose induced by neutrons of different energy groups inside water layers of different thicknesses.

4.1.2 Photon doses in water

Photons due to neutron interactions with the experiment materials were simulated over a wide energy spectrum (

Figure 4-8) in the energy group structure of BUGLE-80. Maxima are found for the prompt photons following neutron capture in Hydrogen (2.2MeV) and Lead (7.4MeV). Furthermore, pair production followed by positron annihilation is observed at 511keV.

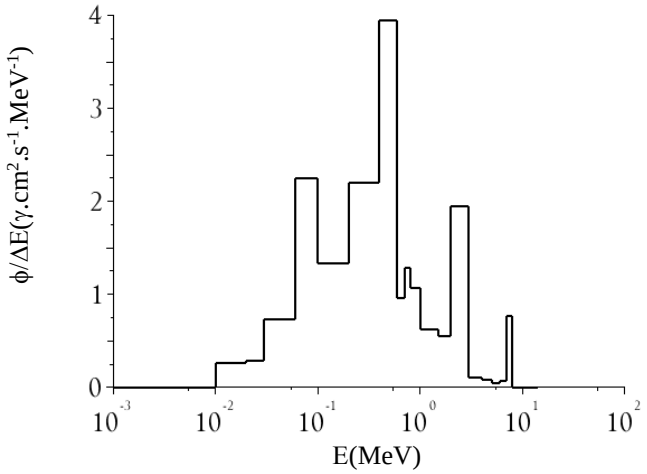

Figure 4-8 Photon fluence rate (in γ.cm^{-2}.s^{-1}.MeV^{-1}) in the experience box, normalized to 1MW reactor power.

Photon doses in water were calculated using the F6 and the dose modified *F4 tally using the photon mass absorption coefficient of photons in water (Figure 4-9). Figure 4-10 displays a non-negligible contribution from low-energy photons due to their high mass absorption coefficient. A value of 166mGy.h^{-1}/MW (±1.5%) was obtained with both tallies. For comparison with TLD measurements expressed in air, the corresponding dose in air given: 151mGy.h^{-1}/MW (

Figure 4-10). Simulations of the cell samples yield an increased photon dose of 253mGy.h^{-1} (±1.3%) in air.

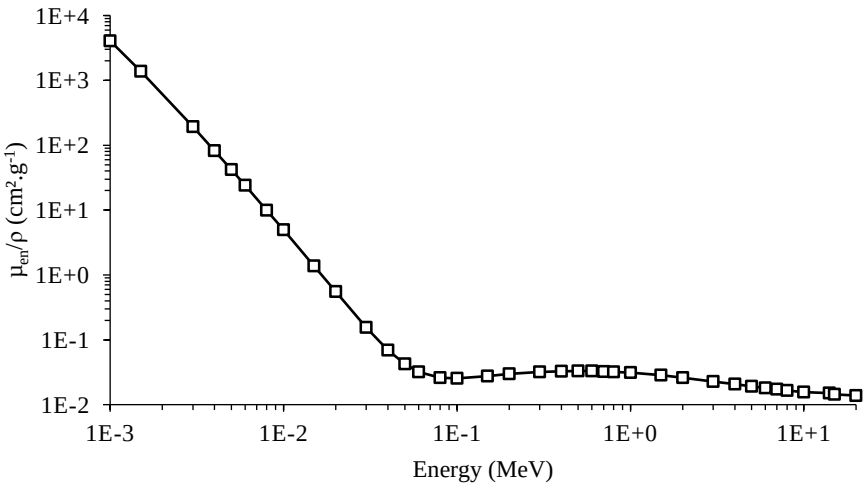

Figure 4-9 Photon mass absorption coefficient in water input in the MCNP model, obtained from NIST.

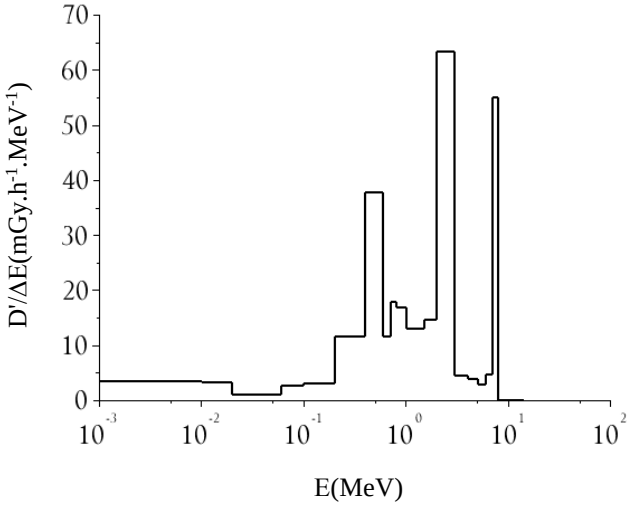

Figure 4-10 Photon-dose rate in water (in mGy.h^{-1}MeV^{-1}/MW), in the experience box normalized to 1MW reactor power

4.2 Measured neutron fluence rates

4.2.1 Efficiency of the HPGe gamma spectrometer

The efficiency curve of the gamma spectrometer is presented in Figure 4-11. A polynomial fit in two energy regions was made, yielding a detector efficiency of 0.184% for the 411keV of ^{198}Au. The efficiency ratio between 14.5 and 1.0 cm source-detector distance 18.93, averaged over 5 measurements.

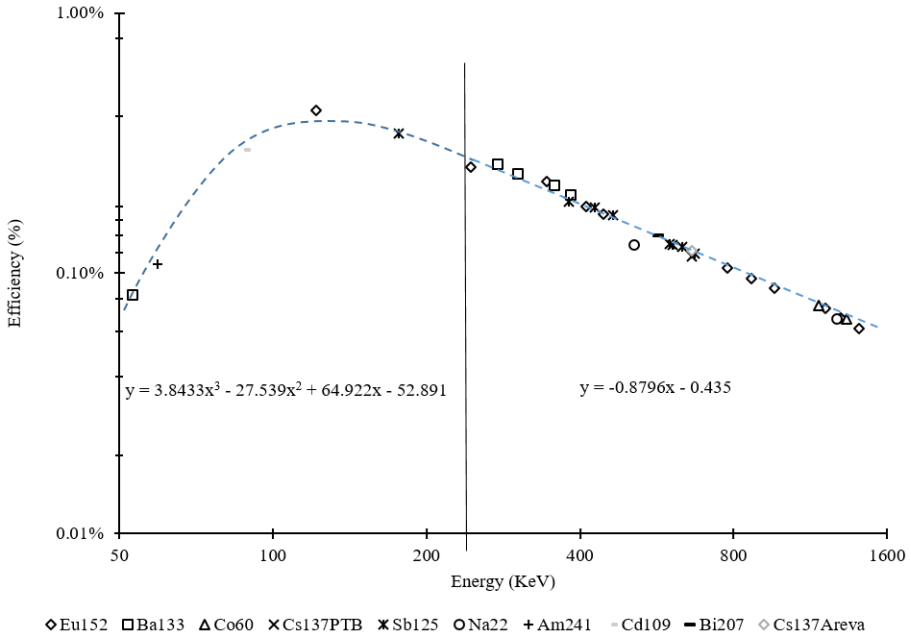

Figure 4-11 Efficiency to energy response curve of the HPGe detector used, note the log axis.

4.2.2 Neutron fluence rates in the irradiation box

Thermal and epithermal neutron fluences were measured by the Cadmium-ratio method using two separate irradiations of bare and Cd-covered foils. The calculated self-shielding factors for the Au detectors are: G_{th}=0.96, G_{epi}=0.28. For G_{epi}, resonance data was extracted from ENDF B-VII.1.

The neutron fluence distribution in the irradiation box was measured in the transversal and longitudinal directions. Seventeen bare Au foils were distributed in the irradiation box forming a cross parallel to the 2 axes and irradiated for 4 hours. The distribution of epithermal neutron fluence employed 15 Cd-covered foils irradiated for 8h. The distributions of the thermal and epithermal neutron fluence rates are plotted with the distance to the centre of the box (Figure 4-13 and Figure 4-12).

The neutron flux is constant within 7% along the x axis of the experience box. A slight increase is observed on the sides of the box, as the Plexiglas wall may reflect surrounding neutrons. Along the y axis decrease of the flux is visible, with approximately 2.5%/cm for the thermal component from (9.67 to 5.24)x10^7 ncm^{-2}s^{-1}.

Table 4-2 displays the calculated and measured thermal fluence rates in the irradiation box. The standard deviation of the 4 simulations with different seed random numbers was in the order of 0.5% and is included in the uncertainty. The agreement between measurement and calculations is 15%. This value is generally acceptable considering an intrinsic accuracy of 10% for neutron transport simulations, the application of theoretical models describing neutron spectra and the uncertainty in the self-shielding factors.

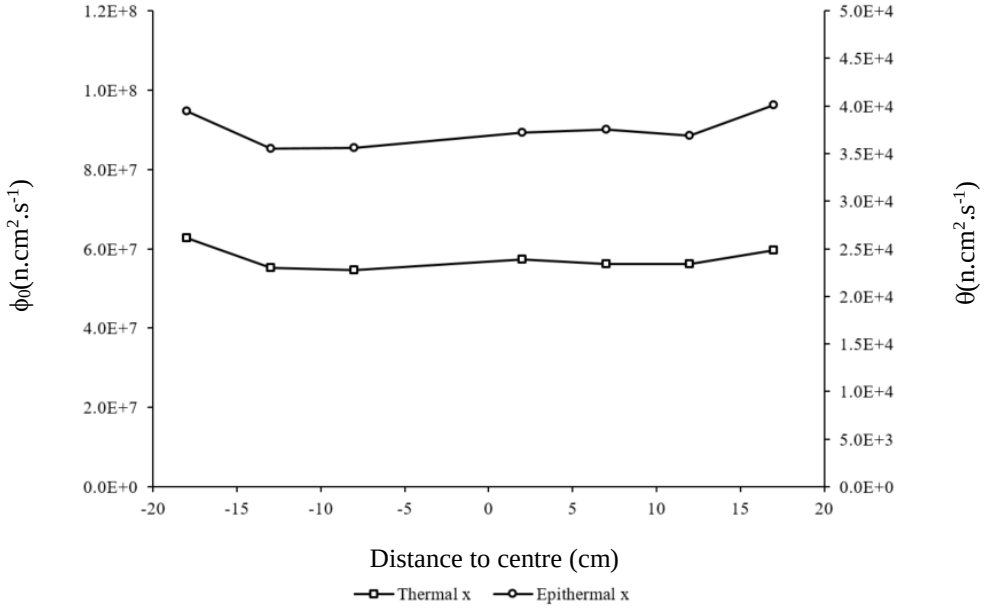

Figure 4-12 Neutron fluence rate distribution along the x axis, normalized at 1MW reactor power.

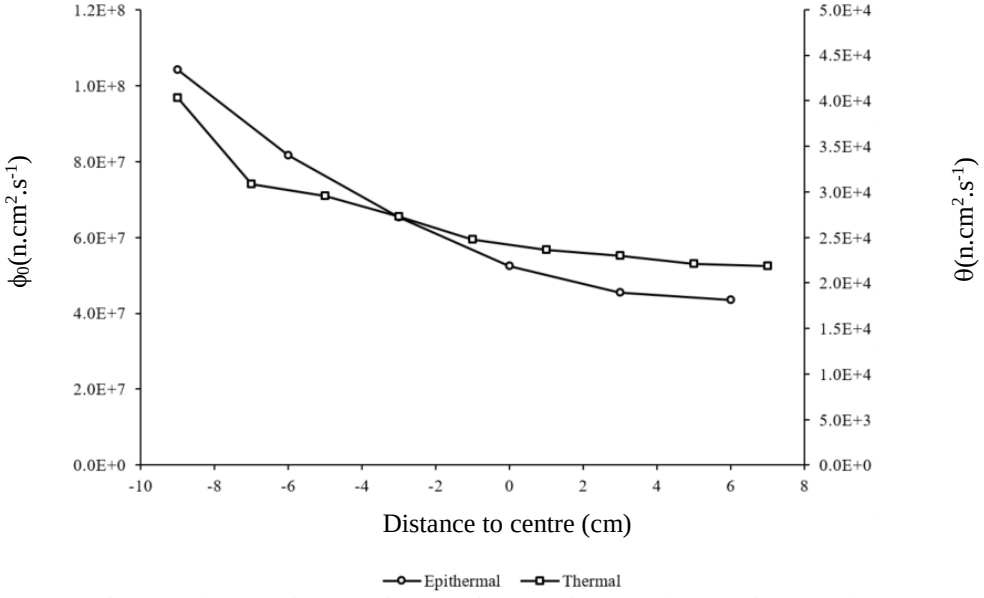

Figure 4-13 Neutron fluence rate distribution on the y axis, normalized at 1MWreactor power.

Table 4-2 Comparison of simulated and measured values for thermal neutron fluence rate.

	$\phi_0(ncm^2s^{-1})$	ε (%)
calculated	$7.59x10^7$	4.31
measured	$6.56x10^7$	3.00

For epithermal neutrons, a steeper longitudinal distribution along cross the y axis relative to thermal neutrons is found. The difference between calculated and measured epithermal fluence rate is 22% (Table 4-3).

The measured thermal to epithermal fluence rate ratio is higher than calculated. This discrepancy indicates that an increased Boron equivalent contamination should be considered due to the presence of other impurities in the graphite and /or lead:

- Chlorine is normally found in graphite (up to 30ppm) due to the manufacturing process. Chlorine has a large absorption thermal cross section and could reduce further the thermal neutron yield
- The hygrometry of the graphite pile was not assessed and could overmoderate the fast neutrons increasing the epithermal component
- Lead filters and shields may also contain several percent of antimony, tin, and other additives used to obtain better mechanical characteristics, leading to spectrum modifications

Table 4-3 Comparison of simulated and measured epithermal neutron fluence rate per unit lethargy θ and their respective relative uncertainties ε.

	θ ($ncm^{-2}s^{-1}$)	ε (%)
calculated	1.96×10^4	9.64
measured	2.40×10^4	3.00

4.3 Photon dosimetry

Photon dose was assessed across the irradiation box using TLD-500 and TLD-700H pairs on 17 positions, irradiated for 3h. Using the previously obtained thermal neutron distribution, it was possible to derive the local neutron fluence Φ_{th} endured by each TLD set. The signal induced by the neutrons was deduced from the raw measurements D_γ; the corrected gamma dose in air $D_{\gamma c}$ is given by:

$$D_{\gamma c} = D_\gamma - \left(\frac{3.5}{1 \times 10^{10}} \times \Phi_{th}\right) \quad \text{(eq.36)}$$

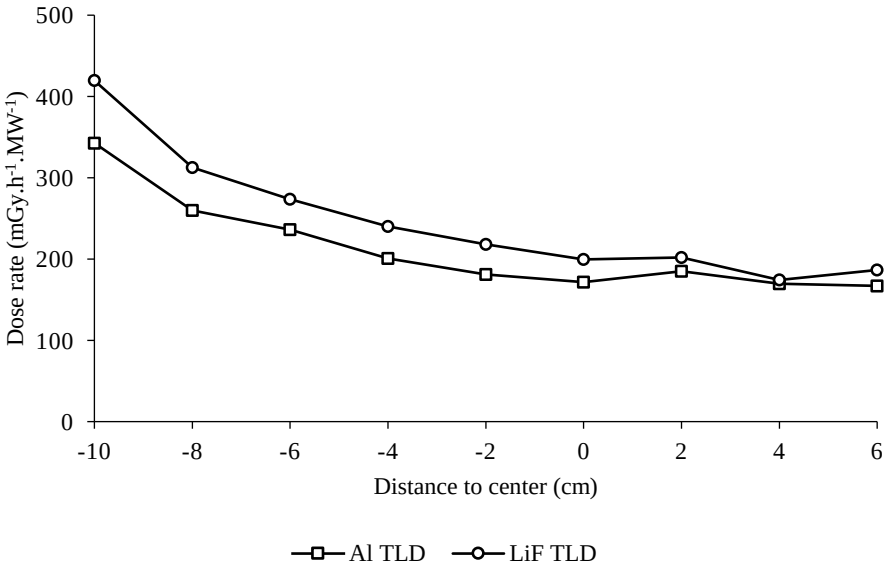

Figure 4-14 Photon dose profile on the y axis.

As for neutrons, a higher dose rate is expected on the closest side to the reactor core (Figure 4-14). On the transversal axis x, no relevant fluctuation of the photon dose rate was observed, confirming the indivisibility of neutron and photon components (Figure 4-15).

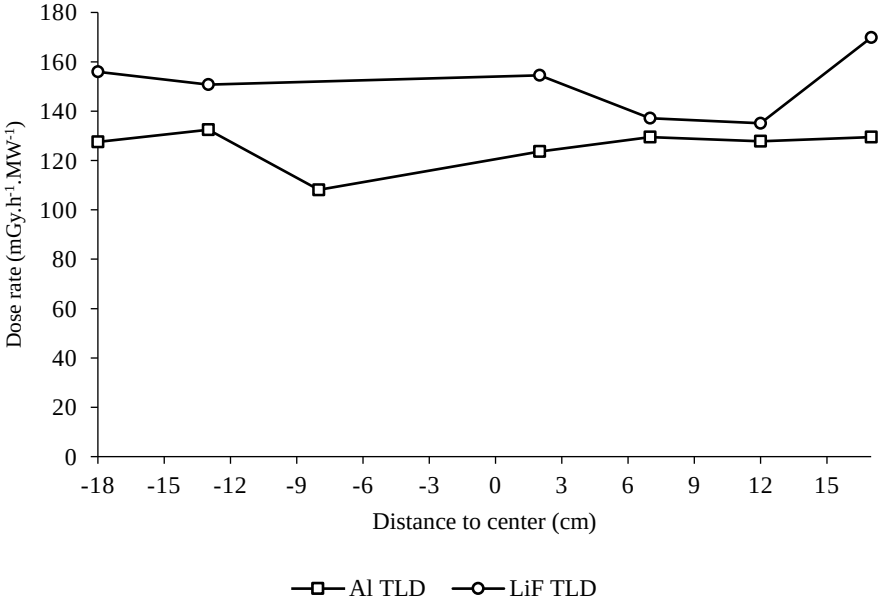

Figure 4-15 Photon dose profile on the x axis

TLD-700H yields a systematically higher photon dose (by 14%) over TLD-500, which can be due to the application of nominal neutron sensitivity values. From this, an uncertainty of 10% is estimated for the photon dose measurements retrieved by the average results with both materials. Gamma dose in air shows an agreement of 95% between simulations and measures (Table 4-4) that is clearly smaller than the measurement uncertainty.

Table 4-4 Comparison of simulated and measured values for photon dose rate D'_γ and their respective relative uncertainties ε.

	D'_γ (mGyh^{-1})	ε (%)
simulated	151.0	1.50
measured	158.6	7.56

4.4 Reproducibility of the irradiation conditions

Fluctuations in the average neutron fluence rate among different irradiations are normally encountered due to e.g., poisoning, control rod insertion and operation. According to the ^{16}N monitoring system (annex 0) the reactor power during 13 irradiations in the thermal column varied from 600 to 734kW. From the 5 gold monitors at fixed positions in the irradiation box, the response of that in the center exhibited an appreciable influence from the culture flasks (annex 0) and has been therefore discard. The average response of monitors at the box corners is able to track the reactor power within ±3%; this value sets the reproducibility of the irradiation conditions apart from power variations.

The homogeneity of the neutron fluence and photon dose in the transversal direction is better than 3% and 6%, respectively.

4.5 GEANT4 simulation of cell doses

About 10^5 neutrons in each energy group (thermal, epithermal and fast) were generated, in addition to 10^6 photons, leading to a total of 462 interactions within the cell culture layer. Table 4-6 shows the contribution of the various radiations to the cell dose. The energy deposited by the incident photon component is negligible, similarly to the epithermal and fast neutron contributions. The BNC reaction induces >95% of the total dose (Table 4-6). The dose rate at 1 MW reactor power is 602mGyh^{-1} for an equivalent boron concentration of 25ppm. This value is ~5 times larger than retrieved by a simplified theoretical calculation. In order to understand this effect, a series of simulations were performed for considering B dispersed in an air layer (to avoid self-shielding and scattering from the medium), Boron in a 1mm-thick water layer in the culture flask with a (10x10)cm^2 neutron source and a similar set-up with a (50x50)cm^2 source that embarks the Lead shield and irradiation box. The results (Table 4-5) show that such an agreement is destroyed by the scattering in the flask+medium materials.

Table 4-5 Comparison of analytical and Monte Carlo dose in a boron volume

	Analytical dose (Gy.ncm^2/^{nat}B ppm)	*Simulated dose (Gy.ncm^2/^{nat}B ppm)*	*Ratio (Simulated/Analytical)*
Boron in air	1.66E-14	1.59E-14	0.96
Boron in water, (10x10 cm source)	1.66E-14	8.41E-14	5.05
Boron in water, (50x50 cm source)	1.66E-14	1.10E-13	6.62

Table 4-6 shows the contribution of the various radiations to the cell dose. The energy deposited by the incident photon component is negligible relative to the lithium and alpha recoils, similarly to the epithermal and fast neutron contributions. The BNC reaction induces >95% of the total dose. If higher (>25 ppm) boron concentrations are encountered, the contribution of the BNC to the dose will be even larger, as fast and epithermal neutrons, as well as photon reactions are independent to the boron amount in the culture.

Table 4-6 Contribution of the different primaries to the overall deposited energy in the cell layer (Gy/ncm^{-2})

	^{7}Li	*electrons*	*alphas*	*gammas*	*protons*	*nuclei*	*TOTAL*	*Contribution(%)*
n_{th}	7.70E-13	3.59E-15	1.34E-12	3.37E-16	8.63E-21	5.59E-22	2.11E-12	95.87
n_{epi}	7.95E-15	8.81E-18	1.39E-14	2.51E-18	4.38E-21	5.14E-23	2.19E-14	0.99
n_{fast}	1.71E-14	1.27E-15	2.01E-14	0.01%	1.71E-14	1.27E-15	2.01E-14	0.91
γ	0.00E+00	4.90E-14	0.00E+00	5.88E-19	0.00E+00	0.00E+00	4.90E-14	2.22
							2.20E-12	100

4.5.1 Dose in cell structures

The simulation considered 10^6 thermal neutrons incident on a layer of fifteen U87 cells (within a volume of $100\mu m^3$). The doses received by the nucleus and cytoplasm of a single cell were calculated, in conditions similar to the actual experiment (Figure 4-16).

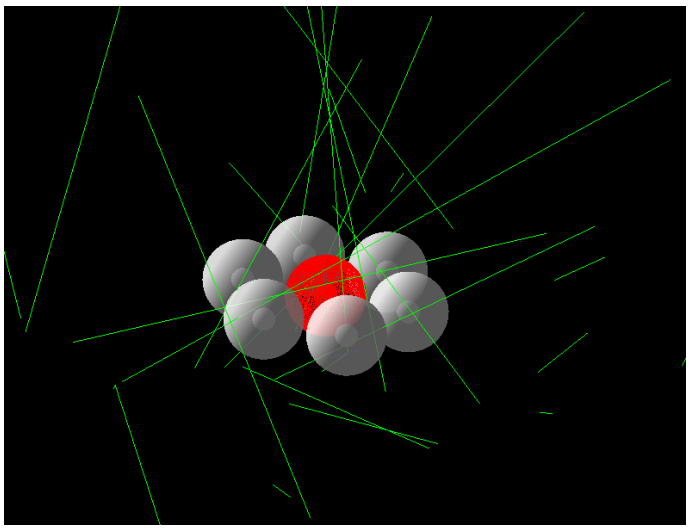

Figure 4-16 Geometry of the microdosimetric model, 25 neutrons are generated, some cells were hidden, the central is sensitive

According to ICP-MS, there is a total cell uptake of 1187ppm ^{nat}B, of which 15% is in the nucleus and 85% in the ensemble membrane+cytosol+cytoskeleton (Table 4-7). The dose received by the central cell is about 60Gy for a thermal neutron flux of $4x10^{12}$ $n.cm^{-2}$. No relevant difference is observed whether only the central cell or all cells are loaded with Boron. In an extreme situation of a cell medium containing a high amount of boron (10 000ppm), the dose in the cytoplasm is increased by 0.8%. The dose in the cell is therefore induced mainly from the incorporated compound.

Table 4-7 GEANT4 simulation dose results of the microdosimetric model in different configurations (D) with respective relative uncertainty (ε), for $4x10^{12}$ $n_{th}.cm^{-2}$.

	Cell average		*Cell nucleus*		*Cell cytosplasm&cytosol*	
Boron loading	D(Gy)	ε(%)	D(Gy)	ε(%)	D(Gy)	ε(%)
Central cell	59	5.98	36.8	11.95	58.7	5.72
All cells	60.5	5.75	35.7	12.22	56.4	5.78

Table 4.8 sums up the calculated and simulation results doses, normalized to boron content and neutron flux. The agreement between analytical calculations and doses measured in a cell nucleus differs by several orders of magnitude.

Table 4-8 Normalized dose of macrodosimetric and microdosimetric models (Gy.ncm^2/^{nat}B ppm)

			Microdosimetric model		
	Analytical	*Global model*	*Cell average*	*Cytoplasm*	*Nucleus*
Dose rate	1.66E-14	1.10E-13	1.27E-14	1.33E-18	2.44E-19
Agreement with analytical calculations	1.00	6.62	0.77	8.01E-5	1.47E-5

The inhomogeneity of the boron concentration inside the cell compartments, as well as a mean free path of the particles higher than the nucleus dimensions render microdosimetric Monte-Carlo simulations mandatory over macrodosimetric models or analytical simplified calculations.

4.6 BNC experiments

4.6.1 Toxicity of the compound

The cytotocixity of CMA appears to be very low at low concentrations. At the largest concentration (200µM), 88% of the cells survived after 4 hours of incubation (Figure 4-17).

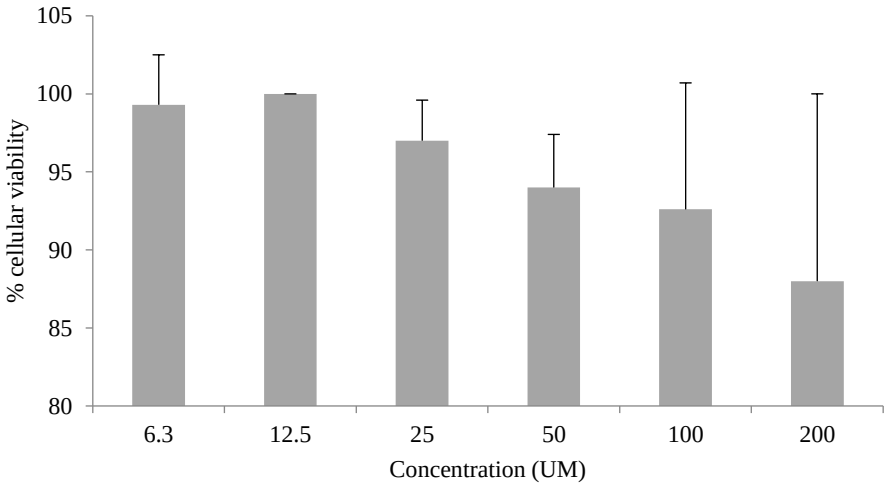

Figure 4-17 Cellular viability upon 6h treatment with carboranylmethylbenzoacridone

4.6.2 Boron repartition in the cell structures

Figure 4-18A gives the amount of ^{11}B present in the cells, fractionated in membranes, cytoskeleton, cytosol and nucleus. Figure 4-18B shows the ^{11}B absolute repartition in the cell layers.

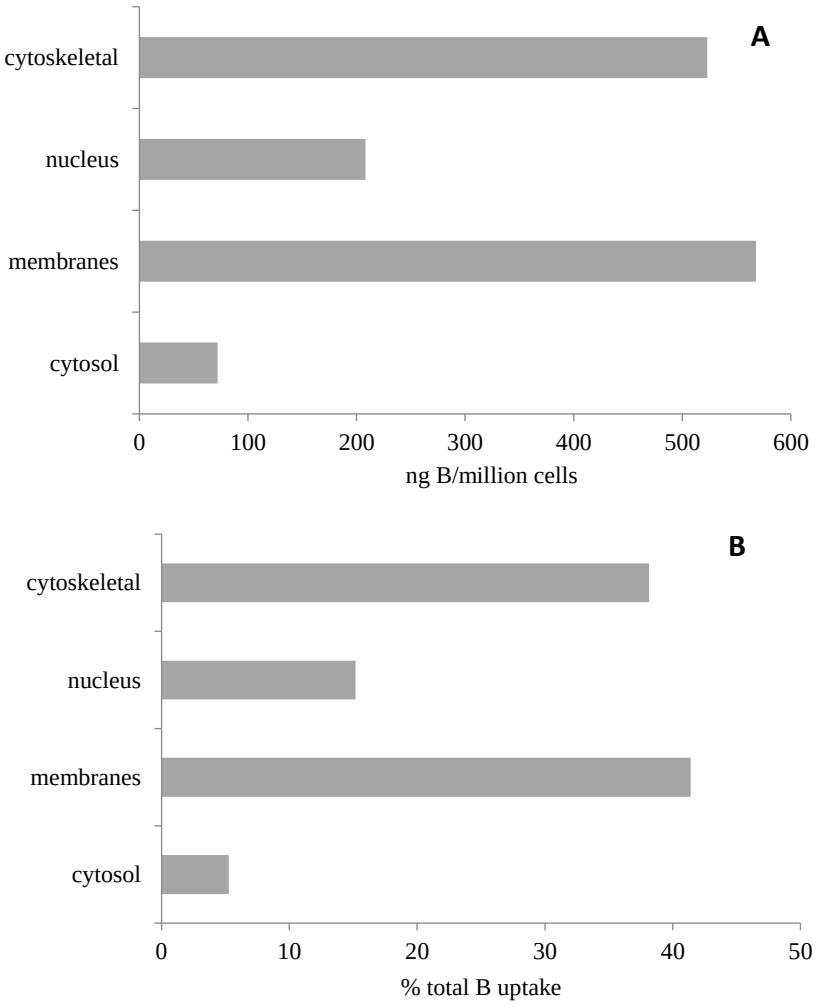

Figure 4-18 Cellular distribution of carboranylmethylbenzoacridone in the U87 cells, upon 1 h treatment at 350uM. Results show the boron content in the cellular fractions are expressed as: (A) ng B/10E6 cells and (B) % total B uptake

Carboranylmethylbenzoacridone can be more observed in the membranes and in the cytoskeleton of the cells. Only 15% of the boronated compound enter the nucleus. The overall uptake of natural boron per cell as high as 1187ppm at a CMA concentration of 350μM.

4.6.3 Radiotoxicity of the BNC reaction

The effect of the neutrons on the CMA incubated culture cells population is very strong (Figure 4-19). The cultures' populations decrease to 21% at the highest concentration. Non-incubated but irradiated cells barely suffer from the mixed field, with 92.5% survival after 72h.

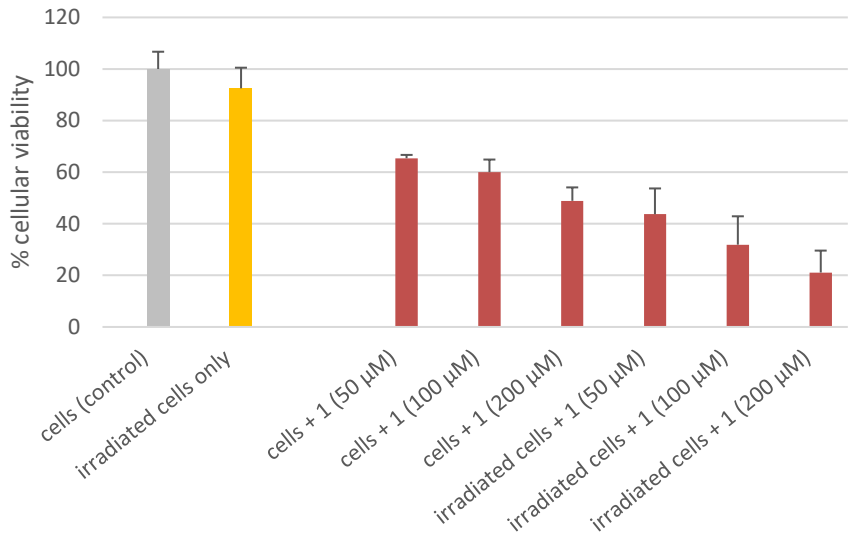

Figure 4-19 Cellular viability (%) of U87 cells after neutron irradiation for compound 1(carboranylmethylbenzoacridone) during 4h30 at 720kW after 72h recovery

4.6.3.1 Early damages

According to fluoroscopy pictures (Figure 4-20), CMA mainly rests in the cell's cytoskeleton. The typical fibre-like pattern observed in green shows the compound location, this visual inspection corroborates the ICP-MS results. With such optical microscope, the membrane of the cell (≈4nm) is not visible.

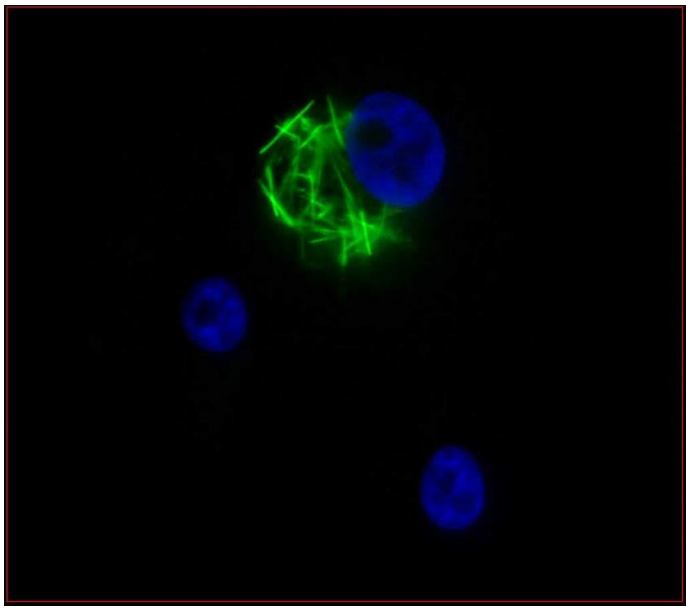

Figure 4-20 Fluoroscopy picture of U87 cells post-irradiation, blue is the nucleus, green is the compound carboranylmethylbenzoacridone. Note the repartition in the cytoskeleton

DSB appear to occur mainly on the cells successfully incubated by carboranylmethylbenzoacridone (Figure 4-21). On cells having successfully absorbed CMA, several DSB are visible. Even if the medium contained most of the compound (>99%), few DSB are observable in non-receptive cells.

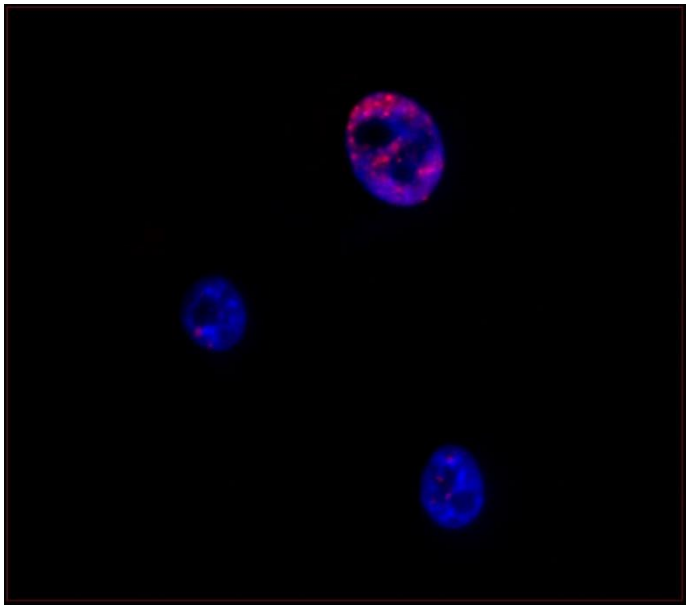

Figure 4-21 H2AX assay shows DSB occurrences on red areas. These are the 3 same cells as on the fluoroscopy picture

A comparison of results obtained with the various compounds showed that a predominant incorporation of the compound in the nucleus is not critical for the effectiveness of the BNC reaction, in contrast to early assumptions and corroborated by independent studies (Chouin et al., 2009).

4.6.3.2 Late damages

Micronucleus rate is higher for cells being incubated and irradiated (Figure 4-22). Up to 19% of the culture displays MN for the highest concentration of CMA (100µM). Irradiated cells are also subjected to MN, with a 11% occurrence for the culture placed in the reactor field. Carboranylmethylbenzoacridone has a low impact on MN manifestation if no irradiation occurs.

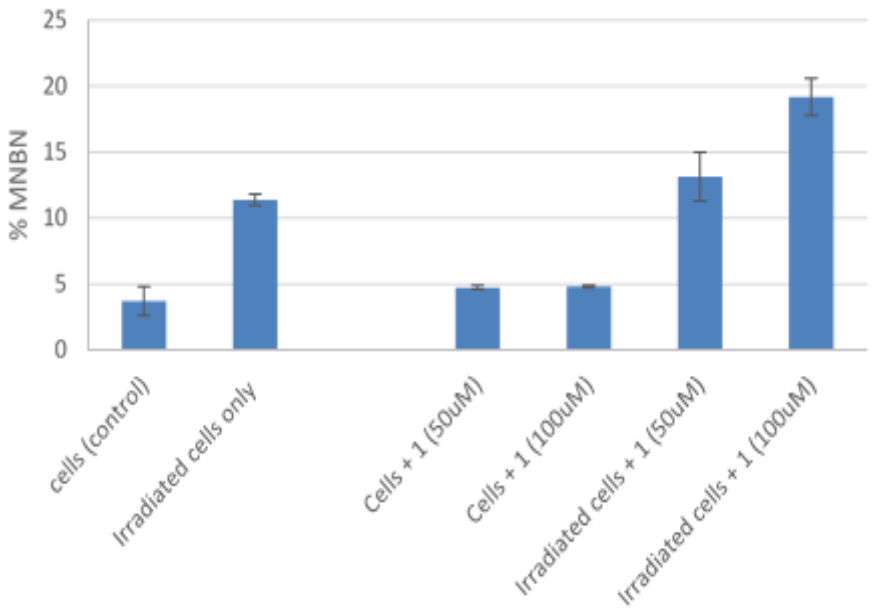

Figure 4-22 Micronucleus occurrence on control and incubated, irradiated cells with (carboranylmethylbenzoacridone) after 72h recovery

The response of BNC depends on the boron concentration inside the target cells. Even if the medium is saturated by boron compound, all cells are not affected by the surrounding alpha and lithium fragments. Gamma dose, emitted by the thermal column and the experience box does not lead to high cell death: blank irradiated cells mostly survived and could reproduce with few late damages. Most of the damages were observed on cells incubated and irradiated, and most the cell deaths can be attributed to the boron reaction fragments generated inside the cells.

4.6.4 Neutron fluence and photon dose in cell irradiations

The reactor power fluctuated between 599kW to 734kW during the 5 biological irradiations, leading in a variation of the thermal neutron fluence rate in the irradiation box. The total fluence under the culture flasks was between (3.22 to 8.21)x10^{11} ncm^{-2} including the perturbation induced by the sample (section 4.1.1). In one irradiation TLDs were placed under the cell-bearing containers. The measurements (Table 4-9) show an increase of the local gamma dose by 68%, in accordance (94%) with the simulations (section 4.3).

Table 4-9 Photon dose measurements during BNC experiments

Configuration	*Dose with Al_2O_3 TLD (mGy/h)*	*Dose with LiF TLD (mGy/h)*
No boronated compound	141	176
Culture flask (200uM)	262	296
Culture flask (0uM)	294	320
Well plate (200uM)	320	330

Even if boron is present is small quantities on the other side of the experience box, the local photon flux is disturbed. On the same position, an increase of 35% with Al_2O_3:C TLD and 28% with ^{7}LiF:CuPMg TLD is noticed if boron is present in the experience box. The increase is even larger (up to 59%) for culture flasks loaded with high boron concentrations.

5 Conclusion

A Monte Carlo model of the thermal column of the RPI has been developed and employed towards the investigation of the radiation field at the facility. A 10ppm Boron-equivalent contamination of the graphite was determined upon comparison with activation measurement. Simulated and measured outputs within ±15%, ±22% and ±5% for thermal neutrons, epithermal neutron and photons, respectively. This level of agreement is considered satisfactory in integral neutron fluence and photon dose measurements for reactor dosimetry. The Monte Carlo model of the experimental setup shows that the BNC reaction contributes with more than 95% of cell doses, allowing to simplify the irradiation dosimetry and microdosimetric model.

From microdosimetric simulations, the dose received by each cell with a compound concentration of 350μM and exposed to a thermal neutron fluence of 8.20×10^{11} $n_{th}cm^{-2}$ (corresponding to an irradiation at maximum reactor power for ~3h) is 12Gy.

The lack of agreement between microdosimetric Monte Carlo simulations and analytical calculations demonstrates the need of precise cell models for dose estimations.

The carboranylmethylbenzoacridone compounds employed in this work have low cytotoxicity. Some are able to carry large amounts of boron (up to 2.06×10^{10} atoms of ^{10}B) into the cell. For these, a population death reaching 80% over non-irradiated and/or non-incubated cell cultures. The incorporation of the compound into the cell is a necessary condition to achieve radiotoxicity. Once this requirement is fulfilled, the effectiveness of the BNC reaction is undeniable. The uptake of the compound by the nucleus does not seem to be critical, as double strand breaks and late damage are observed in its absence while still incorporated in other cell compartments.

6 References

ABTA, 2012. *Glioblastoma and malignant Astrocytoma.* [Online] Available at: http://www.abta.org/secure/glioblastoma-brochure.pdf [Accessed 2016].

Agostinelli et al, S., 2003. GEANT4: A simulation toolkit. *Nuc. Inst. and Meth.,* 506, p. 250.

Albornoz et al., A., 2005. Characterisation of a neutron beam available at the RPI using a set of Bonner spheres. *Radiat. Prot. Dosimetry,* 116, p. 77.

Alcober et al, V., 1997. The BNCT Technique Applied to Cell Cultures. Microdosimetric Calculations. *Proceedings of the XXVI Reunion Bienal de la Real Sociedad Espanola de Fisica.*

Allison, J. a. a., 2006. Geant4 developments and applications. *IEEE Transactions on Nuclear Science,* 53, p. 270.

Barth et al, R., 2005. Boron Neutron Capture therapy of cancer: current status and future prospects.. *Clin. Cancer Res.*,11, p. 3897.

Barth et al, R., 2009. Boron neutron capture therapy at the crossroads: challenges and opportunities.. *Appl. Radiat. Isot.*,7, p. 67.

Bernal et al., M., 2015. Track structure modeling in liquid water: A review of the Geant4-DNA very low energy extension of the Geant4 Monte Carlo simulation toolkit. *Physica Medica,*31, p. 861.

Blue et al, T., 2003. Accelerator based epithermal neutron sources for boron neutron capture therapy of brain tumors. *Neurooncol,* 62, p. 19.

Bussac, J., 1978. *Traité de Neutronique: Physique et calculs des réacteurs nucléaires (...).* Paris: Hermann.

Castro, C. e., 2009. *Instalaçao de um sistema de registo continuo para controlo da potencia do rpi usando actividade de N-16,* ITN.

Caswell, 1980. Kerma Factors for Neutron. *Radiation Research.*

Chouin et al., N., 2009. Evidence of extranuclear cell sensitivity to alpha-particle radiation using a microdosimetric model. I. Presentation and validation of a microdosimetric model.. *Radiat Res.,* 171, p. 657.

Coderre, 1999. The Radiation Biology of Boron Neutron. *Radiat. Res.,* 151, p. 1.

Crossley, 2007. Boronated DNA-binding compounds as potential agents for boron neutron capture therapy. *Medicinal Chemistry,* 7, p. 303.

DaSilva et al, A., 2014. Synthesis, characterization and biological evaluation of carboranylmethylbenzo[b]acridones as novel agents for boron neutron capture therapy. *Org. Biomol. Cheme,* 12, p. 5201.

Fernandes et al., A., 2010. Validation of the Monte Carlo model supporting core conversion of the Portuguese Research Reactor (RPI) for neutron fluence rate determinations. *Ann. Nucl. Energy,* 37, p. 1139.

Fernandes, A., 2003. *Dosimetria de campos mistos de radiação no reactor portugues de investigação: simulação de monte carlo e dosimetria por termoluminescência,* s.l.: Universidade de Lisboa.

Gonçalves et al, I., 1998. *Monte Carlo calculations for enhancement of the epithermal component of the neutron field in the thermal column of the RPI for BNCT,* s.l.: Int. Conf. on Physics of Nuclear Science and Technology.

Gonçalves, I., 1997. Use of the Thermal Column of the Portuguese Research Reactor (RPI) for BNC Therapy. *4th meeting on Nuclear Applications, Brasil.*

Gonçalves, I., 1997. Work in the field of BNCT using the Portuguese Research Reactor. *Jour. Radioanal. Nuc. Chem..*

Gonçalves, I., 1998. Monte Carlo calculations for enhancement of the epithermal component of the neutron field in the thermal column of the RPI for BNCT. *Int. Conf. on Physics of Nuclear Science and Technology.*

IAEA, 1977. *Neutron Fluence Measurements.* Vienna: IAEA.

IAEA, 1985. *Neutron Monitoring for Radiological Protection.* Vienna: IAEA.

Irles et al., A., 2001. A biological study on the effects of high and low LET radiations following boron neutron capture reaction at the Portuguese Research Reactor. *Phys. Med,* 17, p. 17.

Le Sech, C., 2014. *Physique Nucléaire Des quarks aux applications.* 2nd ed. Paris: Dunod.

Lemaignan, C., 2004. *Sciences des Matériaux pour le Nucléaire.* Les Ulis: EDP Sciences.

Li et al, Y., 2010. Start up of the first in hospital neutron irradiator (IHNI1) & presentation of the BNCT development status in China. *Proceedings of the 14th Int Congress on Neutron Capture Therapy,* p. 371.

Lin et al, C., 2003. The conditional probabilities of survival in patients with anaplastic astrocytoma or glioblastoma multiforme.. *Surg. Neurol.,* 60, p. 402.

Lomakin et al, S., 1967. Measurements of Neutron temperature by means of Lutecium isotopes. *Soviet Atomic Energy,* 24, p. 484.

Los Alamos, 1997. *MCNP Manual Vol2.* s.l.:s.n.

Lu et al., D., 1997. Selective boron drug delivery to brain tumors for boron neutron capture therapy. *Adv. Drug Delivery Rev,* 26, p. 231.

Martinho et al., E., 2003. Universal curve of epithermal neutron resonance self-shielding factors in foils, wires and spheres. *Applied Rad. and Isot.,* 58, p. 371.

Martinho et al, E., 2004. Universal curve of thermal neutron self-shielding. *Journal of Radioanalytical and Nuclear Chemistry,* 261, p. 637.

Moss, R., 2014. Moss R.L. Critical review, with an optimistic outlook, on Boron Neutron Capture Therapy (BNCT).. *Appl. Radiat. Isot.,* 88, p. 2.

Mukawa et al., T., 2011. Study on microdosimetry for boron neutron capture therapy. *Nuc. Sci. and Tech.,* 2, p. 242.

NEA, 2016. *Java-based Nuclear Data Information System.* [Online] Available at: http://www.oecd-nea.org/janis/

OEEC-NEA, 1959. *Nuclear Graphite.* Bournemouth: OEEC.

Oliveira et al., N., 2001. Effect of poly(ADP-ribosyl)ation inhibitors on the genotoxic effects of boron neutron capture reaction.. *Mutation Research,* 583, p. 36.

Oliveira, 2000. Genotoxic effects of boron neutron capture reaction in human melanoma cells.

Oliveira, J., 2005. *O Reactor Nuclear Portugues.* Lisboa: O Mirante.

Oliveira, N., 2001. Evaluation of the genotoxic effects of the boron neutron capture reaction in human melanoma cells using the cytokinesis block micronucleus assay. *Mutagenesis.*

Palisade Corporation, 2016. *@RISK Manual.* 7.5 ed. Ithaca: s.n.

PerkinElmer, 2015. *The 30 Minutes guide to ICP-MS.* [Online].

Podgorsak, E., 2005. *Review of Radiation Oncology Physics: A Handbook for Teachers and Students,* Vienna: IAEA.

Reuss, P., 2003. *Précis de Neutronique.* Les Ullis: EDP Sciences.

Riley et al, K., 2003. Performance characteristics of the MIT fission converter based epithermal neutron beam. *Phys. Med. Biol.,* 48, p. 943.

Serra et al., V., 2010. New porphyrin amino acid conjugates: synthesis and photodynamic effect in human epithelial cells.. *Bioorg. Med. Chem.,* 18, p. 6170.

Sinclair et al, W., 1992. Relative Biological Effectiveness (RBE), Quality Factor (Q), and Radiation Weighting Factor (wR). *Annals of the ICRP,* 33.

Stecher-Rasmussen et al., F., 1997. A code of practice for the dosimetry of BNCT in Europe. *Proceedings of 7th international symposium on neutron capture therapy.*

Sterbentz, J., 2013. *Q-Value (MeV/fission) Determination for the Advanced Test Reactor.* Idaho Falls: Idaho National Laboratory.

Thornton et al, D., 2016. The EWGRD Round Robin Measurement Exercice. *EPJ Web of Conference,* 106.

Treille, C. &., 1963. *Précis d'énergie nucléaire.* Paris: Dunod.

Tsoulfanidis N., L. S., 1995. *Measurements and detection of radiations.*CRC Press.

Wirtz, B. &., 1964. *Neutron Physics*.

Yohioka et al., M., 2014. Construction of an accelerator-based bnct facility at the ibaraki neutron medical research center. *Proceedings to LINAC 2014,* p. 230.

Annexes

Monitors factors and constants

	Dimensions	*Gth*	*<Gres>*	*g*	*Fcad*	*σ(2200m/s)*	*I*	*Alu. %*
^{197}Au	⌀50µm 6mm	0.959	0.280	1.005	1.008	98.8b	1570b	0
^{197}Au	⌀5 µm 12mm	0.996	0.671	1.005	1.008	98.8b	1570b	0
^{nat}In	⌀12.7mm 12um	0.888	0.228	1.021	1	169.5b	2624b	0
^{nat}W	⌀12.7mm 150um	0.985	0.248	1.001	1	37.5b	518b	0
^{175}Lu	⌀12.7mm	1	1	1	1	23.1b	621b	97.58
^{176}Lu	⌀12.7mm	1	1	1	1	2097b	920b	97.58

Observed reactions

Nuclear reaction	*Decay, daughter*	*Obs γ(keV)*	*P_γ*	*$T_{½}$ (m)*
$^{197}Au(n,\gamma)\ ^{198}Au$	β- ^{198}Hg	411.8	98.99	3880.8
$^{115}In(n,\gamma)\ ^{116m1+2}In$	β- ^{116}Sn	1097, 1293	56.20, 84.40	54.0
$^{186}W\ (n,\gamma)\ ^{187}W$	β- ^{187}Re	479, 685	21.8, 27.3	1423.2
$^{164}Dy\ (n,\gamma)\ ^{165}Dy$	β- ^{165}Ho	95	3.6	140.0
$^{175}Lu\ (n,\gamma)\ ^{176m}Lu$	β- ^{176}Hf	88	14.5	218.1
$^{176}Lu\ (n,\gamma)\ ^{177m}Lu$	β- ^{177}Hf	208	10.36	9662.4

Fluence rate and power measured during experiments

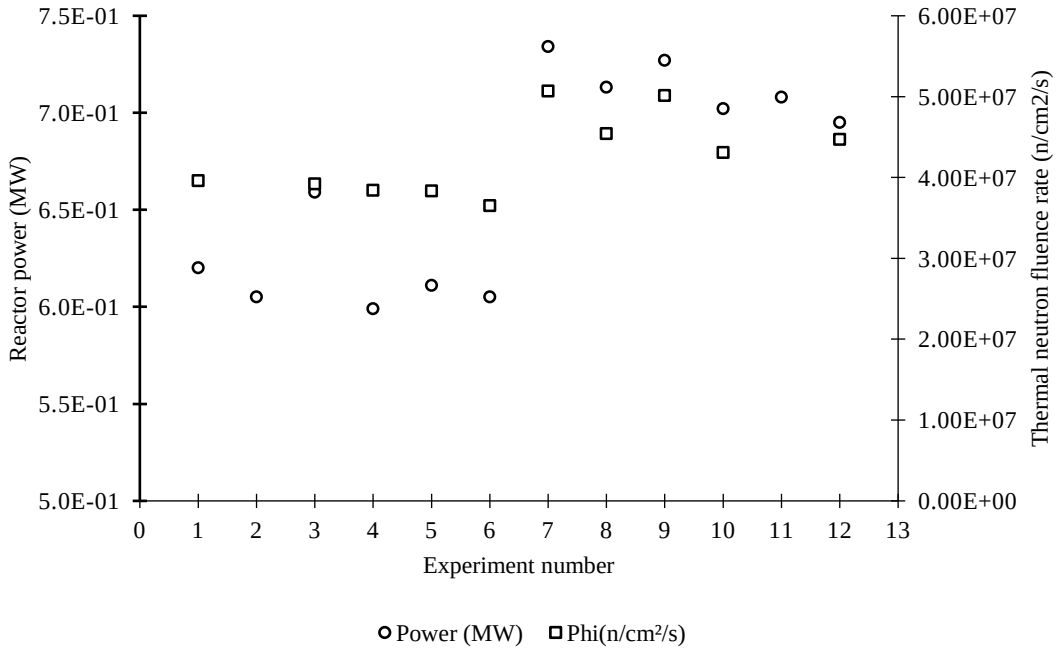

Gold detector responses during cells irradiations

Irr.	1	3	4	5	6	7	8	9	10	12		
rb1/kw	7.64E-15	6.94E-15	7.47E-15	7.49E-15	6.96E-15	7.65E-15	7.48E-15	7.96E-15	6.79E-15	7.64E-15		
rb2/kw	7.50E-15	6.97E-15	7.42E-15	7.41E-15	7.08E-15	7.93E-15	7.52E-15	8.03E-15	7.45E-15	7.55E-15		
rb3/kw	5.98E-15	5.49E-15	6.56E-15	5.98E-15	5.69E-15	7.87E-15	5.81E-15	7.73E-15	5.76E-15	6.42E-15		
rb4/kw	4.66E-15	4.52E-15	4.71E-15	4.52E-15	4.51E-15	4.76E-15	4.65E-15	4.68E-15	4.58E-15	4.49E-15		
rb5/kw	4.74E-15	4.56E-15	4.47E-15	4.58E-15	4.61E-15	4.79E-15	4.70E-15	4.57E-15	4.74E-15	4.61E-15	<rb/kW>	σ(%)
<rb/kW>	6.14E-15	5.75E-15	6.02E-15	6.00E-15	5.79E-15	6.28E-15	6.09E-15	6.31E-15	5.89E-15	6.07E-15	6.03E-15	3.10

Irradiations specifications

#	Date	ϕ_{th}(ncm^{-2}.s^{-1})	Power (MW)	Start	Stop	Time	Purpose
1	28-03-16	3.96E+07	0.620	14:47	19:00	4:13	Thermal variation
2	30-03-16		0.605	11:33	19:37	8:04	Epithermal variation
3	05-04-16	3.92E+07	0.659	10:27	18:28	8:01	Epithermal normalization
4	12-04-16	3.84E+07	0.599	11:43	16:27	4:44	BNCT#1 cp1&2
5	15-04-16	3.83E+07	0.611	11:48	16:19	4:31	BNCT#2 cp1&2&3
6	19-04-16	3.65E+07	0.605	14:46	18:19	3:33	TLD+ spectrum unfolding
7	21-04-16	5.07E+07	0.734	11:26	16:02	4:36	BNCT#3 cp1&2&3
8	22-04-16	4.54E+07	0.713	10:48	15:53	5:05	Spectrum unfolding Cd
9	27-04-16	5.01E+07	0.727	11:50	16:25	4:35	BNCT#4 cp1&2 +Lu+TLD
10	28-04-16	4.31E+07	0.702	10:56	15:28	4:32	Epithermal #2 + Fast + Lu
11	02-05-16		0.708	20:42	21:45	1:03	Core irrad for HpGe efficiency
12	04-05-16	4.47E+07	0.695	12:13	14:12	1:59	BNCT#5 cp1&2+Lu

Considered gamma peaks for HpGe calibration

Energy (keV)	Emission Probability per decay
^{22}Na (950.57d ±0.23d)	
511	1.798
1274.537	0.9994
^{60}Co (1925.23d ±0.27d)	
1173.228	0.9985
1332.492	0.999826
^{109}Cd (461.4d ±1.2d)	
88.0336	0.03626
^{125}Sb (1007.48d ±0.21d)	
176.314	0.0682
380.452	0.0152
427.874	0.2955
463.365	0.1048
600.597	0.1776
606.713	0.0502
635.95	0.1132
671.441	0.01783
^{133}Ba (3848.7d ±1.2d)	
53.1622	0.0214
79.6142[1]	0.0265
80.9979[1]	0.329
276.3989	0.0716
302.8508	0.1834
356.0129	0.6205
383.8485	0.0894
^{137}Cs (10990d ±4d)	
661.657	0.8499
^{152}Eu (4941d ±7d)	
121.7817	0.2841
244.6974	0.0755
344.2785	0.2658
411.1165	0.02237
443.965	0.03125
778.9045	0.1296
867.38	0.04241
964.072	0.1462
1085.837	0.1013
1089.737	0.01731
1112.076	0.134
1212.948	0.01415
1299.142	0.01632
1408.013	0.2085
^{207}Bi (11800d ±300d)	
569.698	0.9776
^{241}Am (157580d ±230d)	
59.5406keV[2]	0.3578

[1] Not considered due to resolution

[2] Lower energy peaks could not be detected

Detail of the thermal column assembly of the RPI

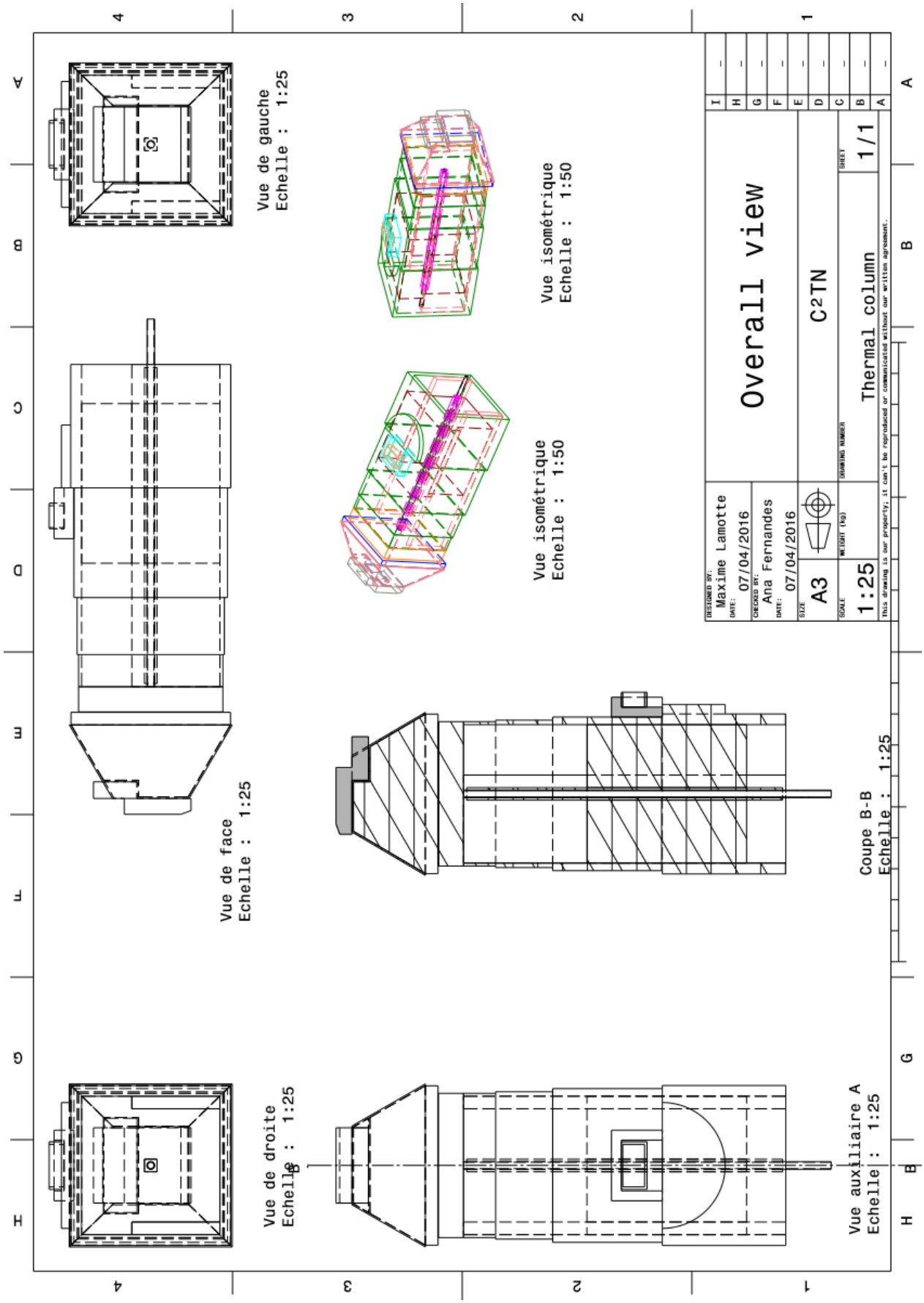

CAD model of the experience box

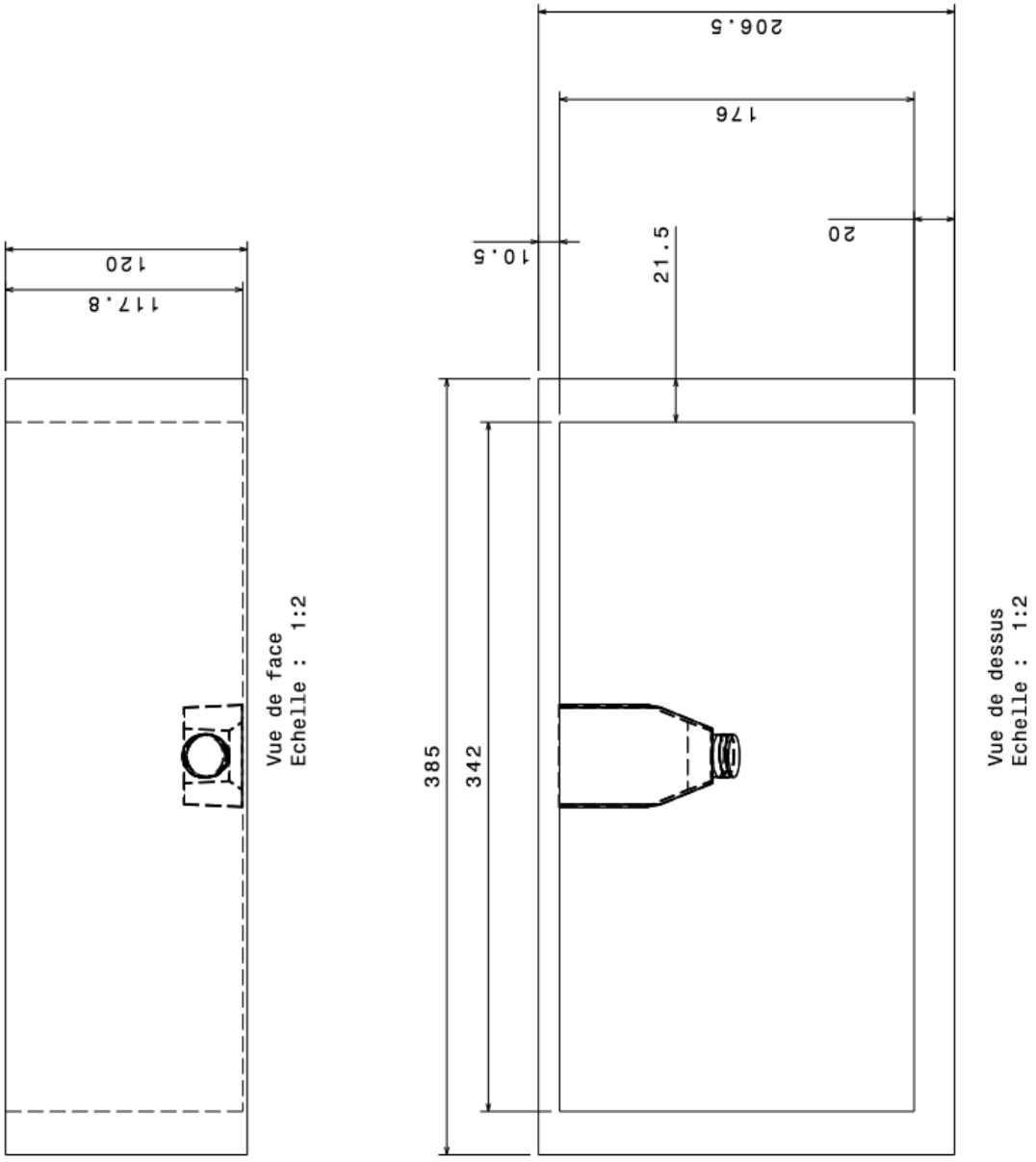

CAD model of the culture flask